

# 1 Navigating the complexity of detrital rutile provenance:

## 2 Methodological insights from the Neotethys Orogen in Anatolia

3 Megan A. Mueller<sup>1,2,\*</sup>, Alexis Licht<sup>1,3</sup>, Andreas Möller<sup>4</sup>, Cailey B. Condit<sup>1</sup>, Julie C. Fosdick<sup>2</sup>, Faruk  
4 Ocakoglu<sup>5</sup>, Clay Campbell<sup>6</sup>

5 <sup>1</sup>. Department of Earth and Space Sciences, University of Washington, 4000 15th Avenue NE, Seattle, WA 98195, USA

6 <sup>2</sup>. Department of Earth Sciences, University of Connecticut, 354 Mansfield Road - Unit 1045, Storrs, CT 06269, USA

7 <sup>3</sup>. Aix-Marseille Université, CNRS, IRD, INRAE, Collège de France, CEREGE, Technopôle de l'Arbois-Méditerranée, BP80,  
8 13545 Aix-en-Provence, France

9 <sup>4</sup>. Department of Geology, The University of Kansas, 1414 Naismith Drive, Lawrence, KS 66045, USA

10 <sup>5</sup>. Department of Geological Engineering, Eskişehir Osmangazi University, Büyükdere, 26040 Eskişehir, Türkiye

11 <sup>6</sup>. Department of Geosciences, University of Arizona, 1040 E 4th St, Tucson, AZ 85721, USA

12 \* Now at Department of Earth and Planetary Sciences, Jackson School of Geosciences, The University of Texas at  
13 Austin, 2305 Speedway Stop C1160, Austin, TX 78712, USA

14 *Correspondence to:* Megan Mueller (megan.mueller@jsg.utexas.edu)

15 **Abstract.** Sedimentary provenance is a powerful tool for reconstructing convergent margin evolution. Yet single mineral  
16 approaches, like detrital zircon, have struggled to track sediment input from mafic and metamorphic sources. Detrital rutile  
17 complements detrital zircon datasets by offering a path forward in sedimentary provenance reconstructions where metamorphic  
18 terranes are potential source regions. However, U-Pb geochronology in rutile can be difficult due to low uranium  
19 concentrations and incorporation of common Pb, and multiple workflows are currently in use. Here, we investigate U-Pb and  
20 trace element data reduction, processing, and common Pb correction workflows using new detrital rutile U-Pb geochronology  
21 and trace element geochemistry results from the Late Cretaceous to Eocene Central Sakarya and Sarıcakaya Basins in Anatolia.  
22 A significant number of analyses were rejected (54%) due to signal intensity limitations, namely low U, low Pb, anomalous  
23 signal, and inclusions. We identify this as a universal limitation of large-*n* detrital rutile studies and recommend the systematic  
24 reporting of the amount of discarded analysis and the processes for rejection in all studies using detrital rutile U-Pb  
25 geochronology. Additionally, we show that (1) the <sup>208</sup>Pb and <sup>207</sup>Pb common Pb reduction schemes produce similar age  
26 distributions and can be used indifferently; (2) The Stacey-Kramers distance is a suitable metric for quantifying U-Pb  
27 discordance but a discordance filter is not recommended; (3) Instead, filtering U-Pb data by a power law function based on  
28 corrected date uncertainty is appropriate; (4) The exclusion of low uranium concentration rutile biases date distributions and  
29 favors pelitic-derived, higher Zr-in-rutile temperature, higher U-Pb concordance grains; (5) Paired U-Pb and trace elements

30 can be used to evaluate potential bias in U-Pb data rejection, which reveals that data rejection does not bias the provenance  
31 interpretations; (6) [The](#) signature of sediment recycling can be identified through U-Pb dates and Zr-in-rutile temperatures.  
32 To better navigate the complexity of detrital rutile datasets and to facilitate the standardization of data reporting approaches,  
33 we provide open access code as Jupyter Notebooks for data processing and analysis steps, including common Pb corrections,  
34 uncertainty filters, discordance calculations, and trace element analysis.

## 35 **1 Introduction**

36 Sedimentary provenance analysis is widely used to reconstruct ancient sediment dispersal networks, source-to-sink  
37 sediment budgets, sedimentary basin evolution, and to discern links between tectonics, geodynamics, paleogeography, climate,  
38 and biologic evolution (Dickinson and Suczek, 1979; Garzanti et al., 2007; Clift et al., 2008; Gehrels, 2014; Blum and Pecha,  
39 2014). Compositional provenance methods include sediment petrologic, chemical, and heavy mineral characterizations (e.g.,  
40 Gazzi, 1965; Hubert, 1971; Dickinson and Suczek, 1979; Morton, 1985; Garzanti and Andò, 2007). Over the last several  
41 decades, the rise of chronometric and geochemical techniques led to the increase in single-mineral approaches. Detrital zircon  
42 U-Pb geochronology has become the most widely used technique as zircon is refractory and is abundant in crustal rocks (e.g.,  
43 Gehrels, 2014). Further, the age, thermal history, and elemental and isotopic composition of detrital zircons can quantitatively  
44 reconstruct both sedimentary provenance and geodynamic, tectonic, and magmatic processes (Carrapa, 2010; Paterson and  
45 Ducea, 2015; Tang et al., 2020; Sundell et al., 2022). However, one major limitation is that zircons predominantly form in  
46 intermediate to felsic magmas, thus detrital zircon suites generally lack information about mafic igneous and metamorphic  
47 processes and sources (Hietpas et al., 2011; Moecher et al., 2011; Gaschnig, 2019). Zircon is present in metamorphic rocks as  
48 inclusions in other minerals or as recrystallized-dissolved-reprecipitated rims on zircon cores (Kohn and Kelly, 2017). The  
49 outer growth domains of zircons can be targeted with laser ablation ICP-MS depth profiling, or with spot analysis if the rims  
50 are thick enough, yet the most commonly used techniques for rapid provenance data acquisition do not routinely analyze zircon  
51 rims. Therefore, sedimentary provenance interpretations based on detrital zircon alone are incomplete. For this reason the  
52 sedimentary provenance community is increasingly turning to U-Th-Pb and trace elements in phases commonly used in  
53 petrochronology, such as detrital rutile (Zack et al., 2004a; Meinhold, 2010; Triebold et al., 2012; Bracciali et al., 2013; Rösel  
54 et al., 2014, 2019; O'Sullivan et al., 2016; Odlum et al., 2019; Pereira et al., 2020), detrital apatite (Morton and Yaxley, 2007;  
55 Chew et al., 2011; Mark et al., 2016; O'Sullivan et al., 2016, 2020), detrital monazite (Hietpas et al., 2010; Moecher et al.,  
56 2011; Gaschnig, 2019), and detrital titanite (Guo et al., 2020; Chew et al., 2020), in addition to other isotopic systems in these  
57 and other detrital minerals.

58 Detrital rutile is a complementary sedimentary provenance proxy to detrital zircon. Rutile forms in metamafic and  
59 metapelitic rocks across a range of P-T conditions, therefore, detrital rutile is especially advantageous when tracking sediment  
60 input from greenschist to eclogite or granulite facies sources (e.g., Meinhold, 2010; Zack and Kooijman, 2017). The  
61 geochemical composition [of rutile](#) can further distinguish between metamorphic protoliths (e.g., Triebold et al., 2007, 2012;

62 Meinhold, 2010). However, rutile U-Pb analysis is challenging due to low U and low radiogenic Pb concentrations and due to  
63 the incorporation of initial non-radiogenic Pb. Here, we use a new detrital rutile petrochronology dataset from Anatolia to  
64 investigate data reduction, processing and analytical steps in order to support robust provenance interpretations. In a number  
65 of studies, analyses have been discarded during U-Pb data reduction due to unacceptable signal intensity (e.g. Bracciali et al.,  
66 2013; Rösel et al., 2014, 2019), and we find that discarding analyses is a limitation to large-*n* detrital rutile datasets in the  
67 literature and this study. We test the sensitivity of resulting U-Pb date spectra to Pb correction methods, uncertainty and  
68 discordance filters, and a low U cutoff threshold. Ultimately, the new dataset demonstrates that detrital rutile captures sediment  
69 input from a subduction accretion complex that is poorly resolved in the detrital zircon record. Despite the described  
70 limitations, detrital rutile petrochronology can be effectively used to reconstruct sedimentary provenance ~~and sediment~~  
71 ~~recycling~~, deformation, ~~and~~ metamorphism, ~~and sediment recycling~~.

## 72 **2 Detrital Rutile Provenance**

### 73 **2.1 Detrital Rutile Synopsis**

74 The advantages of detrital rutile provenance are extensively documented (e.g., Zack et al., 2004a; Meinhold, 2010;  
75 Triebold et al., 2012; Bracciali, 2019; Gaschnig, 2019; Pereira et al., 2020; Pereira and Storey, 2023) so we provide only a  
76 brief overview here. Rutile is the most common TiO<sub>2</sub> polymorph, a common accessory mineral in metamorphic and igneous  
77 rocks (Meinhold, 2010; Zack and Kooijman, 2017), and an abundant heavy mineral in sedimentary rocks (Morton, 1985).  
78 Rutile is present across a range of P-T conditions: rutile is generally stable at the surface and medium- to high-grade  
79 metamorphic conditions. Rutile can readily crystallize from titanite, ilmenite and biotite during prograde metamorphism  
80 (Luvizotto et al., 2009; Meinhold, 2010; Cave et al., 2015). The breakdown of rutile to titanite occurs in prograde and  
81 retrograde environments, particularly in sub-greenschist to lower greenschist facies where titanite stability is favored (Cave et  
82 al., 2015; Zack et al., 2004b). Experimentally, rutile is stable above around 1.2–1.4 GPa in metagranitoids and hydrated basalts  
83 depending on compositional and chemical variability and in some cases can be stable down to 0.7 GPa (Xiong et al., 2005;  
84 Angiboust and Harlov, 2017). In subduction zone settings, rutile is especially abundant in eclogites (Klemme et al., 2002).

85 The chemical composition of rutile preserves original petrogenetic information. Rutile concentrates high field  
86 strength elements (Zr, Nb, Mo, Sn, Sb, Hf, Ta, W) through substitution with Ti that are commonly used as fingerprints of  
87 subduction zone metamorphism and crustal evolution (Foley et al., 2000; Rudnick et al., 2000). Detrital rutile geochemistry  
88 fingerprints the lithologies of sediment sources in several unique ways: rutile concentrates the vast majority of available Nb  
89 whereas Cr is non-selective and is distributed across metamorphic minerals; therefore, the Cr and Nb concentrations in rutile  
90 can discriminate between metamafic and metapelitic lithologies (Zack et al., 2004a, b; Triebold et al., 2011, 2012). Cr and Nb  
91 concentrations are attributed to different protoliths: generally metapelitic rutile (i.e. mica schists, paragneisses, felsic  
92 granulites) have less Cr than Nb contents, and metabasic rutile (i.e., mafic eclogites and granulites) have greater Cr than Nb  
93 contents; ~~generally~~ (Zack et al., 2004b). Additionally, the incorporation of Zr in rutile is largely temperature dependent (Zack

94 et al., 2004b; Watson et al., 2006; Tomkins et al., 2007; Ferry and Watson, 2007). Zirconium mobilizes during prograde  
95 metamorphic fluid release; the incorporation of Zr into rutile is buffered by coexisting quartz and zircon (Zack et al., 2004b).  
96 Zr contents in rutile correlate with peak metamorphic temperature and pressure conditions (Zack et al., 2004b; Watson et al.,  
97 2006; Tomkins et al., 2007; Kohn, 2020). Therefore, the Zr elemental composition in rutile is a commonly used thermometer,  
98 empirically and experimentally calibrated across a range of pressures and thermodynamic activity parameters (Zack et al.,  
99 2004b; Watson et al., 2006; Tomkins et al., 2007; Kohn, 2020). Zircon, quartz and rutile must be in equilibrium to use the Zr-  
100 in-rutile thermometer (e.g., Zack et al., 2004b), an assumption that likely holds in pelitic rocks (Pereira et al., 2021) but may  
101 not in mafic lithologies, yet the assumption is hard to evaluate in a detrital context. Inclusions in rutile can be used to determine  
102 whether rutile grew in equilibrium (Hart et al., 2016, 2018; see also Pereira and Storey, 2023 and references therein). In detrital  
103 rutile, removed from the petrologic system in which they formed, and thereby missing key thermobarometric mineral  
104 associations, the Zr-in-rutile thermometer thus provides an estimate of the minimum peak metamorphic temperatures because  
105 the exact activity of SiO<sub>2</sub> in the original system is unconstrained (Kooijman et al., 2012; Triebold et al., 2012; Pereira et al.,  
106 2021; see also Meinhold et al., 2008; Rösel et al., 2019; Şengün et al., 2020; Zoleikhaei et al., 2021). For rutile of unknown  
107 source lithology, the calculated temperature is affected by the chosen pressure estimate; Pereira and Storey (2023) demonstrate  
108 this pressure dependence in detrital grains and recommend using the experimental and empirical calibration of Kohn (2020);  
109 their eqn. 13) at an average pressure of 13 kbar with an uncertainty of 5 kbar:

$$T \text{ (}^\circ\text{C)} = \frac{71360 + 0.378 \times P - 0.130 \times C}{130.66 - R \times \ln[C]} - 273.15$$

(1)

112 where P is the pressure in bars, C is the concentration of Zr in ppm and R is the gas constant, 8.3144 in J·mol<sup>-1</sup>·K<sup>-1</sup>.

113 Uranium is easily substituted for Ti<sup>4+</sup> in rutile ~~making rutile a suitable mineral for U~~ ~~making rutile a suitable mineral~~  
114 ~~for U-Pb analysis~~. Rutile U-Pb analyses were first performed using thermal ionization mass spectrometry (TIMS) (Schärer et  
115 al., 1986; Mezger et al., 1989; Möller et al., 2000; Schmitz and Bowring, 2003; Kylander-Clark et al., 2008) and have since  
116 been collected with SHRIMP (Clark et al., 2000; Meinhold et al., 2010; Ewing et al., 2015), LA-MC-ICP-MS (Vry and Baker,  
117 2006; Bracciali et al., 2013; Apen et al., 2020), LA-Q-ICP-MS (Storey et al., 2007; Zack et al., 2011), and LA-SC-ICP-MS  
118 (Kooijman et al., 2010; Okay et al., 2011; Smye and Stockli, 2014). As a high-temperature thermochronometer, U-Pb dates in  
119 rutile likely reflect mineral cooling through the closure temperature for volume diffusion of Pb (Dodson, 1973), which is  
120 between 400–640°C in rutile. The temperature sensitivity of this partial retention zone in rutile is dependent on diffusion  
121 kinetics, cooling rate, chemistry, and grain size (Mezger et al., 1989; Cherniak, 2000). Rutile U-Pb dates may correspond to  
122 monotonic cooling from post-magmatic temperatures or cooling from the most recent medium to high-temperature  
123 metamorphic event that exceeded the closure temperature (Zack et al., 2004b; Zack and Kooijman, 2017). Slow cooling rates  
124 can produce rutile U-Pb dates significantly younger than the timing of peak metamorphism (e.g., Möller et al., 2000; Flowers  
125 et al., 2005). Because rutile U-Pb dates record thermal history information from conditions characteristic of the middle to  
126 lower crust (> 400 °C), U-Pb dates are ideal for inferring the timing and rate of deep seated orogenic processes (Mezger et al.,

Formatted: Font color: Black, English (United Kingdom)

127 1989; Möller et al., 2000; Flowers et al., 2005; Kylander-Clark et al., 2008; Smye et al., 2018) and of craton formation,  
128 stabilization and cooling (Davis et al., 2003; Schmitz and Bowring, 2003; Blackburn et al., 2012). Furthermore, detrital rutile  
129 U-Pb geochronology is regularly used in sedimentary provenance analysis to reconstruct sedimentary basin evolution,  
130 paleoclimate and paleoenvironments, and orogen-scale deformation, exhumation, and sediment transport (Rösel et al., 2014,  
131 2019; Mark et al., 2016; O’Sullivan et al., 2016; Pereira et al., 2020; Caracciolo et al., 2021; Clift et al., 2022).

## 132 **2.2 Detrital Rutile U-Pb Challenge #1: Low Uranium Content**

133 Detrital rutile U-Pb petrochronology presents unique analytical, data reduction, and interpretation challenges.  
134 Uranium concentration in rutile varies among metamorphic protoliths: for example, rutile from mafic eclogites tend to have,  
135 on average, 75% less U than those from metapelites (i.e., 5 ppm vs. 21 ppm; Meinhold, 2010). The low U concentrations—  
136 from old rutile or sourced from mafic lithologies (cf. Section 6.2)—can make rutile challenging to date. To optimize data  
137 collection, some detrital rutile methods first analyze trace elements then only collect U-Pb data on rutile above a given U  
138 concentration threshold (ca. > 4–5 ppm; e.g., Zack et al., 2004a, 2011; Okay et al., 2011; Rösel et al., 2019). There is not a  
139 systematic relationship between uranium concentration and common Pb concentration. However, screening low U rutile  
140 reduces the overall length of U-Pb analytical sessions and produces a higher proportion of concordant analyses (Zack et al.,  
141 2004a, 2011; Okay et al., 2011; Rösel et al., 2019). This protocol however introduces bias into the provenance results against  
142 metamafic rocks (cf. Section 6.2), and is generally discouraged (Bracciali et al., 2013; Bracciali, 2019). While this low-U  
143 screening is not necessarily common globally, it is a regional concern. There are 4 published detrital rutile U-Pb datasets from  
144 Türkiye; 2 of the 4 (Okay et al., 2011; Şengün et al., 2020) only analyze U-Pb on detrital rutile with uranium concentrations  
145 above ca. 4–5 ppm. The two studies that do not use a U-threshold filter but instead analyze all detrital rutile grains (Shaanan et  
146 al., 2020; this study) must discard data due to very low uranium signals (below limit of detection). ~~This includes discarding;~~  
147 ~~LOD). The U-threshold filter is intended to maximize the proportion of concordant rutile analyzed. This includes~~ rutile grains  
148 that have low incorporation of U during growth (independent of analytical instrumentation) and rutile grains that have poorly  
149 resolved U-Pb ratios due to low U CPS such as old rutile and mafic rutile (machine dependent). Omitting low U rutile may  
150 make sense in some settings; however, this analytical approach likely biases provenance results as the concentration of uranium  
151 in rutile systematically varies by metamorphic protoliths, with mafic eclogites having lower U contents than metapelites (e.g.,  
152 Meinhold, 2010). This potential bias is important to investigate as metamafic units in suture zones, presumably with low U  
153 rutile, are expected to be a major contributor of detritus to many orogenic basins, including the northwestern Anatolian basins  
154 of this study.

## 2.3 Detrital Rutile U-Pb Challenge #2: Common Pb Incorporation

### 2.3.1 Common Pb Correction Overview

A second challenge with detrital rutile lies with data reduction and presentation. Because many detrital geochronologists are familiar with the zircon system, here we emphasize the differences in how U-Pb data should be treated in common Pb bearing minerals versus zircon. The U-Pb system in rutile is different from that of zircon due to the incorporation of common Pb, thereby requiring careful methodological choices on how to treat non-radiogenic Pb and U-Pb discordance. The zircon U-Pb system is ‘simple’ in the sense that zircon incorporates negligible non-radiogenic initial Pb (i.e., common Pb) or ‘common’ Pb during crystallization, and Pb diffuses only at extremely high temperatures and in zircon with radiation damage (e.g., Schoene, 2014 and references therein). Thus, the majority of detrital zircon U-Pb analyses tend to be close to concordia, which makes data reduction and interpretation fairly straightforward, as even the  $^{207}\text{Pb}/^{206}\text{Pb}$  dates of moderately discordant zircon are likely to be meaningful. Unlike zircon where discordant data exceeding a specified threshold are often discarded, it is not surprising that many rutile analyses may be discordant as rutile can incorporate a significant amount of common Pb. *In-situ* studies mitigate this by: (1) regressing discordia lines through co-genetic analyses in Tera-Wasserburg space, where the lower intercept of the discordia with the concordia defines the U-Pb age of Pb diffusion closure (e.g., Faure, 1986; Chew et al., 2011; Vermeesch, 2020); or (2) applying a non-radiogenic Pb correction either by using an *ad hoc* Pb evolution model such as that of Stacey and Kramers (1975) or by measuring the composition of non-radiogenic Pb in a co-existing phase (e.g. Zack et al. 2004b). However, by nature, co-genetic grains in detrital samples are unknown, and a model therefore has to be applied. Below we review the common Pb correction calculations and discordance metrics for common Pb bearing detrital minerals.

### 2.3.2 $^{204}\text{Pb}$ Correction

The basis of all common Pb correction approaches— $^{204}\text{Pb}$ ,  $^{207}\text{Pb}$  and  $^{208}\text{Pb}$ —is to use a Pb evolution model (e.g., Stacey and Kramers, 1975) to find the fraction of total  $^{206}\text{Pb}$  that is common  $^{206}\text{Pb}$  and, by corollary, find the radiogenic  $^{206}\text{Pb}$  fraction and then calculate the corrected date (Compston et al., 1984; Williams, 1997). We did not measure  $^{204}\text{Pb}$  in this study and refer readers to other publications for  $^{204}\text{Pb}$  correction details (Williams, 1997; Andersen, 2002; Storey et al., 2006; Chew et al., 2014). The  $^{204}\text{Pb}$  correction method is valuable because it uses the non-radiogenic  $^{204}\text{Pb}$  isotope and does not assume concordance, yet accurate measurement of  $^{204}\text{Pb}$  is needed (in contrast, see Andersen, 2002) which can be challenging as  $^{204}\text{Pb}$  is the least abundant Pb isotope. While accurate determination of the low-intensity  $^{204}\text{Pb}$  peak is not a problem for TIMS or MC-ICP-MS instruments (e.g., Simonetti et al., 2005; Gehrels et al., 2008), it can require prohibitively long dwell times in single-collector instruments. Furthermore, the measurement of  $^{204}\text{Pb}$  is complicated by the isobaric interference of  $^{204}\text{Hg}$  introduced in the gas supply. In some cases, the concentration of  $^{204}\text{Hg}$  can be reduced with traps or filters and back stripped by measuring  $^{201}\text{Hg}$  or  $^{202}\text{Hg}$  (e.g., Storey et al., 2006).

### 2.3.3 <sup>208</sup>Pb Correction

The <sup>208</sup>Pb correction method determines the common Pb component using the <sup>232</sup>Th-<sup>208</sup>Pb decay scheme and assumes U-Th-Pb concordance, undisturbed Th/U, and no Pb loss. Because Pb loss is not considered, all corrected dates are (possibly) minimum ages. The <sup>208</sup>Pb correction is ideal for low-Th phases (Zack et al., 2011) and is commonly used for rutile, although not all rutile grains have low Th concentrations and Th contents are often not reported. The equations here are previously described in Williams (1997), Chew et al. (2011), McLean et al. (2011) and as the total-Pb/U-Th scheme in Vermeesch (2020).

The proportion of <sup>206</sup>Pb<sub>common</sub>,  $f_{206}$ , is calculated as

$$f_{206} = \frac{(\frac{^{208}\text{Pb}}{^{206}\text{Pb}})_{\text{measured}} - (\frac{^{208}\text{Pb}^*}{^{206}\text{Pb}^*})}{(\frac{^{208}\text{Pb}}{^{206}\text{Pb}})_{\text{common}} - (\frac{^{208}\text{Pb}^*}{^{206}\text{Pb}^*})} \quad (2)$$

where <sup>208</sup>Pb/<sup>206</sup>Pb<sub>measured</sub> is calculated directly from the raw data. The <sup>208</sup>Pb/<sup>206</sup>Pb<sub>common</sub> ratio is calculated from the two-stage Pb evolution model of Stacey and Kramers (1975) for dates older than 3.7 Ga as

$$\left(\frac{^{206}\text{Pb}}{^{204}\text{Pb}}\right)_{\text{common}} = 7.19 \cdot (e^{\lambda_{238} \cdot 4.57 \times 10^9} - e^{\lambda_{238} \cdot t_i}) + 9.307 \quad (3)$$

and

$$\left(\frac{^{208}\text{Pb}}{^{204}\text{Pb}}\right)_{\text{common}} = 33.21 \cdot (e^{\lambda_{232} \cdot 4.57 \times 10^9} - e^{\lambda_{232} \cdot t_i}) + 29.487 \quad (4)$$

or for dates younger than 3.7 Ga as

$$\left(\frac{^{206}\text{Pb}}{^{204}\text{Pb}}\right)_{\text{common}} = 9.74 \cdot (e^{\lambda_{238} \cdot 3.7 \times 10^9} - e^{\lambda_{238} \cdot t_i}) + 11.152 \quad (5)$$

and

$$\left(\frac{^{208}\text{Pb}}{^{204}\text{Pb}}\right)_{\text{common}} = 36.84 \cdot (e^{\lambda_{232} \cdot 3.7 \times 10^9} - e^{\lambda_{232} \cdot t_i}) + 31.23 \quad (6)$$

where using  $t_i$  is the uncorrected date in years (<sup>206</sup>Pb/<sup>238</sup>U date from the iolite data reduction); the <sup>232</sup>Th decay rate  $\lambda_{232}$  is  $4.9475 \times 10^{-11} \text{ yr}^{-1}$ , and the <sup>238</sup>U decay rate  $\lambda_{238}$  is  $1.55125 \times 10^{-10} \text{ yr}^{-1}$  (Faure, 1986). The expected radiogenic <sup>208</sup>Pb\*/<sup>206</sup>Pb\* ratios are calculated as

$$\frac{{}^{208}\text{Pb}^*}{{}^{206}\text{Pb}^*} = \left( \frac{{}^{232}\text{Th}}{{}^{238}\text{U}} \right) \cdot \left( \frac{e^{\lambda_{232}t_i} - 1}{e^{\lambda_{238}t_i} - 1} \right) \quad (7)$$

Then, the radiogenic component, the  ${}^{206}\text{Pb}^*/{}^{238}\text{U}$  ratio, can be calculated as

$${}^{206}\text{Pb}^*/{}^{238}\text{U} = (1 - f_{206}) \cdot ({}^{206}\text{Pb}/{}^{238}\text{U}_{\text{measured}}). \quad (8)$$

Finally, the  ${}^{208}\text{Pb}$ -corrected date ( ${}^{206}\text{Pb}^*/{}^{238}\text{U}$  date) is calculated by solving the age equation with the  ${}^{206}\text{Pb}^*/{}^{238}\text{U}$  ratio:

$$t_{206} = \frac{1}{\lambda_{238}} \cdot \ln \left( \frac{{}^{206}\text{Pb}^*}{{}^{238}\text{U}} + 1 \right) \quad (9)$$

where  $t_{206}$  is the corrected date in years. The final corrected date is calculated iteratively, whereby each iteration replaces  $t_i$  with the previously calculated  ${}^{206}\text{Pb}^*/{}^{238}\text{U}$  date. [To test the sensitivity of the initial date estimate](#) ~~The final  ${}^{206}\text{Pb}$ -corrected date presented here is from the two hundredth iteration. For our dataset,~~ we varied the initial date estimate, and therefore the initial common Pb composition, from 1 Ma to 1000 Ma and, by the fifth iteration, the resulting  ${}^{208}\text{Pb}$ -corrected date differs by less than 0.05% for 98% of the unknowns. [The final  \${}^{208}\text{Pb}\$ -corrected date presented here is from the two hundredth iteration.](#) The uncertainty on the date is calculated as the equivalent of the percent (propagated) uncertainty of the uncorrected  ${}^{206}\text{Pb}/{}^{238}\text{U}$  ratio (Odlum et al., 2019).

### 2.3.4 ${}^{207}\text{Pb}$ Correction

The  ${}^{207}\text{Pb}$  correction method is based on a linear regression of  ${}^{207}\text{Pb}/{}^{206}\text{Pb}$  and  ${}^{238}\text{U}/{}^{206}\text{Pb}$  in Tera-Wasserburg space (Tera and Wasserburg, 1972) along a two-component mixing line between non-radiogenic and radiogenic Pb (Faure, 1986; 1). This method is most powerful for co-genetic minerals because it does not require knowing  ${}^{207}\text{Pb}/{}^{206}\text{Pb}_{\text{common}}$ . Yet, because co-genetic analyses are inherently unknown in detrital samples, the routine used here calculates the common Pb component of each individual analysis using the Stacey and Kramers (1975) two-stage Pb evolution model and an initial age estimate. The  ${}^{207}\text{Pb}$  correction method assumes U-Pb concordance and no Pb loss but, unlike the  ${}^{208}\text{Pb}$  correction, does not assume an undisturbed U/Th ratio. Because Pb loss is not considered, all corrected dates are (possibly) minimum ages. The equations given here are modified for detrital samples with unknown co-genetic minerals, previously described in Faure (1986), Williams (1997), Chew et al. (2011), and the semitotal-Pb/U scheme of Ludwig (1998) and Vermeesch (2020).

The calculation is similar to the  ${}^{208}\text{Pb}$  correction. First, the proportion of  ${}^{206}\text{Pb}_{\text{common}}$  is calculated as

$$f_{206} = \frac{({}^{207}\text{Pb}/{}^{206}\text{Pb}_{\text{measured}}) - ({}^{207}\text{Pb}^*/{}^{206}\text{Pb}^*)}{({}^{207}\text{Pb}/{}^{206}\text{Pb}_{\text{common}}) - ({}^{207}\text{Pb}^*/{}^{206}\text{Pb}^*)} \quad (10)$$



240 where  $^{207}\text{Pb}/^{206}\text{Pb}_{\text{measured}}$  is taken directly from the raw data. The  $^{207}\text{Pb}/^{206}\text{Pb}_{\text{common}}$  ratio is based on the two-stage Pb evolution  
 241 model of Stacey and Kramers (1975), which is calculated as the ratio of Equation (3) and Equation (11) for dates older than  
 242 3.7 Ga or as the ratio of Equation (5) ~~to~~ and Equation (12) for dates younger than 3.7 Ga:

$$243 \quad \left(\frac{^{207}\text{Pb}}{^{204}\text{Pb}}\right)_{\text{common}} = \frac{7.19}{137.88} \cdot (e^{\lambda_{235} \cdot 4.57 \times 10^9} - e^{\lambda_{235} \cdot t_i}) + 10.294$$

244 (11)

245 or

$$246 \quad \left(\frac{^{207}\text{Pb}}{^{204}\text{Pb}}\right)_{\text{common}} = \frac{9.74}{137.88} \cdot (e^{\lambda_{235} \cdot 3.7 \times 10^9} - e^{\lambda_{235} \cdot t_i}) + 12.998$$

247 (12)

248 where  $t_i$  is the initial date estimate in years and the  $^{235}\text{U}$  decay rate  $\lambda_{235}$  is  $9.8485 \times 10^{-10} \text{ yr}^{-1}$  (Faure, 1986). Here, for  $t_i$  we use  
 249 the  $^{206}\text{Pb}/^{238}\text{U}$  date from the iolite data reduction. However, Chew et al. (2011) demonstrated that the choice of initial date  
 250 results in a  $< 0.05\%$  difference in the final  $^{207}\text{Pb}$ -corrected date after 5 iterations. The expected radiogenic  $^{207}\text{Pb}/^{206}\text{Pb}^*$  ratio is  
 251 calculated as

$$252 \quad \frac{^{207}\text{Pb}^*}{^{206}\text{Pb}^*} = \left(\frac{^{235}\text{U}}{^{238}\text{U}}\right) \cdot \left(\frac{e^{\lambda_{235} t_i} - 1}{e^{\lambda_{238} t_i} - 1}\right)$$

253 (13)

254 where  $^{235}\text{U}/^{238}\text{U}$  is 137.88 (Steiger and Jäger, 1977). Finally, the radiogenic component, the  $^{206}\text{Pb}^*/^{238}\text{U}$  ratio, can be calculated  
 255 using Equation (8) and then used to solve the age equation (Equation (9)). As with the  $^{208}\text{Pb}$  correction, to iteratively calculate  
 256 the date, each iteration replaces  $t_i$  with the previously calculated  $^{206}\text{Pb}^*/^{238}\text{U}$  date. The  $^{207}\text{Pb}$ -corrected date presented here is  
 257 from the two hundredth iteration. The uncertainty on the date is calculated as the equivalent of the percent (propagated)  
 258 uncertainty of the uncorrected  $^{206}\text{Pb}/^{238}\text{U}$  ratio (Odlum et al., 2019). For example, if the initial  $^{206}\text{Pb}/^{238}\text{U}$  ratio has 2%  
 259 uncertainty at 2 sigma and the corrected date is 200 Ma, then the corrected date uncertainty is  $\pm 4 \text{ Ma}$  (2s).

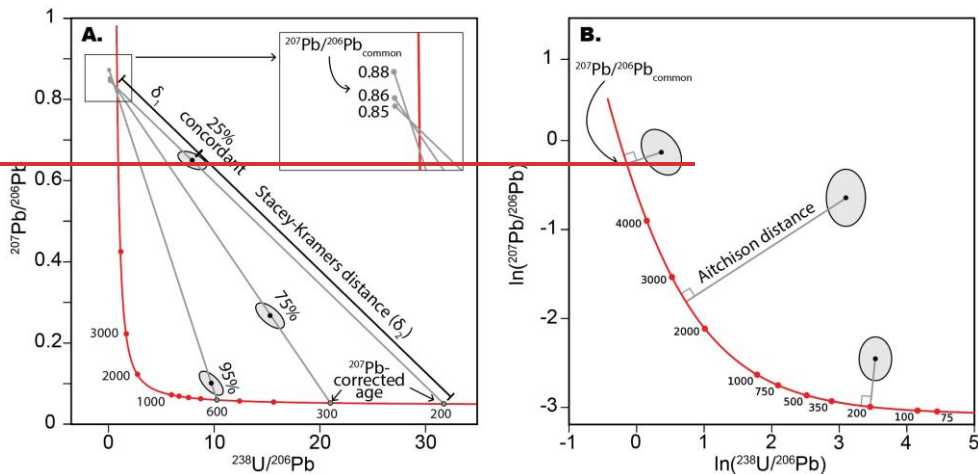
260 **2.3.5 Discordance**

261 Although there are various ways to calculate the discordance of U-Pb analyses, which are reviewed elsewhere (e.g.,  
262 Vermeesch, 2021), it remains unclear which metric is best for common Pb bearing minerals and if a discordance threshold  
263 should be applied. One family of discordance metrics relies on the difference between the  $^{206}\text{Pb}/^{238}\text{U}$  date and  $^{207}\text{Pb}/^{206}\text{Pb}$  date  
264 (e.g., Gehrels, 2011). Because  $^{207}\text{Pb}$  and  $^{208}\text{Pb}$  corrections force concordance, these metrics are not applicable to common Pb  
265 bearing minerals. ~~One metric~~Two metrics potentially relevant to common Pb-bearing minerals ~~is~~are the Stacey-Kramers  
266 distance ~~and Aitchison distance~~ (after Vermeesch, 2021). The Stacey-Kramers distance is calculated by first using the U-Pb  
267 analysis and  $^{207}\text{Pb}/^{206}\text{Pb}_{\text{common}}$  composition (calculated during common Pb correction) to find the discordia in Tera-Wasserburg  
268 space, then discordance is calculated as the distance between the measured  $^{238}\text{U}/^{206}\text{Pb}$  and  $^{207}\text{Pb}/^{206}\text{Pb}$  coordinates and the  
269 concordia intersection ( $\delta_2$ ) along the total discordia line distance ( $\delta_1 + \delta_2$ ) (1; Vermeesch, 2021):

270 
$$\text{Concordance} = \delta_1 / (\delta_1 + \delta_2)$$
  
271 (14)

272 If a discordance threshold is applied, the Stacey-Kramers distance approach includes more young dates than old dates (> 1000  
273 Ma) due to the change in concordia slope around 1000 Ma (Vermeesch, 2021). ~~A second metric is the Aitchison distance~~  
274 (Aitchison, 1982; Pawlowsky-Glahn et al., 2015) ~~which calculates the Euclidean distance from the measured  $^{238}\text{U}/^{206}\text{Pb}$  and~~  
275  ~~$^{207}\text{Pb}/^{206}\text{Pb}$  coordinates to the concordia line in log-ratio Tera-Wasserburg space (1; Vermeesch, 2021). We compare these two~~  
276 ~~metrics with our new dataset. Additionally, detrital zircon studies commonly use a discordance threshold that excludes analyses~~  
277 ~~with discordance above 5–30%, typically around 10% (Spencer et al., 2016), which can induce bias (Nemchin and Cawood,~~  
278 ~~2005; Malusà et al., 2013).~~ The application of a discordance threshold has been underexplored in detrital rutile, with most  
279 studies applying no discordance filter, perhaps due to the lack of consensus on how to define discordance in common Pb  
280 bearing minerals. Rather, a group of studies proposes to filter analyses based on the percent uncertainty of the corrected date  
281 (Mark et al., 2016; Govin et al., 2018; Chew et al., 2020; Caracciolo et al., 2021). It is noted that there is little guidance on  
282 how uncertainties are calculated and propagated during Pb correction, which ought to be investigated in future work;  
283 meanwhile, the filters should be applied with care. We explore these thresholds with our new dataset.

284

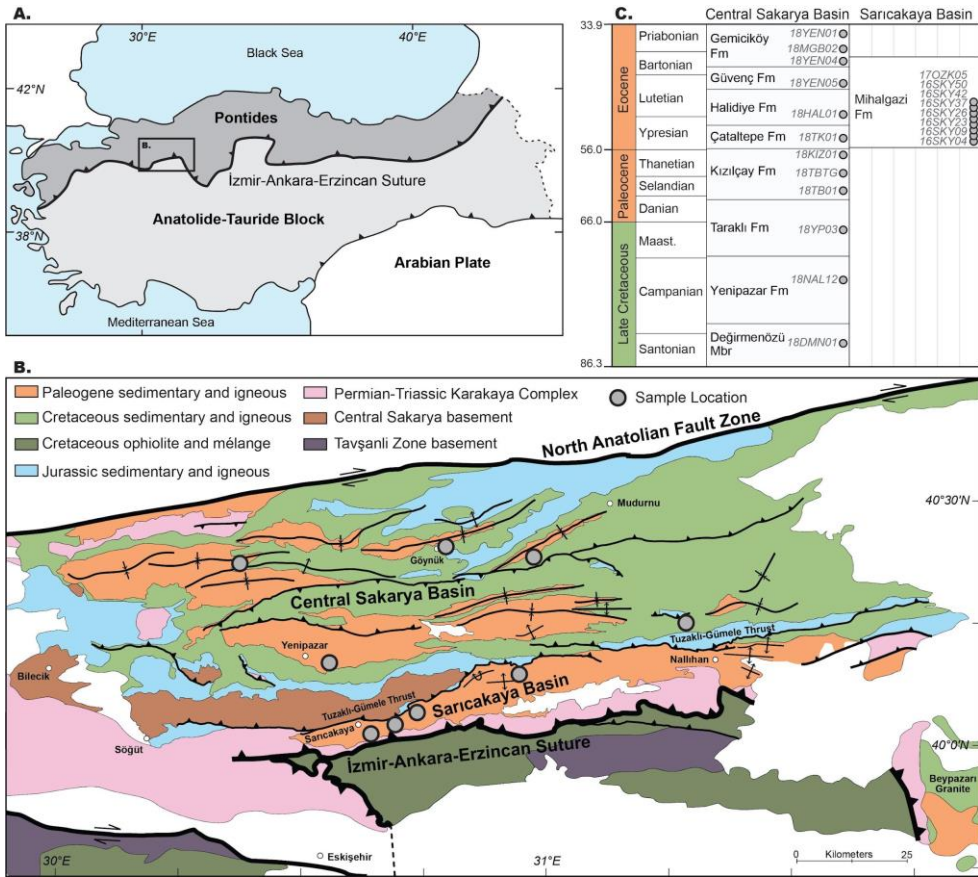


285  
 286 *Figure 1. Conceptual schematics of the  $^{207}\text{Pb}$ -correction and Stacey-Kramers distance (A) and Aitchison distance (B). (A) For*  
 287 *the  $^{207}\text{Pb}$ -correction, first, the common  $^{207}\text{Pb}/^{206}\text{Pb}$  ratio is calculated from the initial date estimate ( $t_i$ ). Next, a discordia is*  
 288 *fitted between  $^{207}\text{Pb}/^{206}\text{Pb}_{\text{common}}$  and the data point. Then, the lower intersection of the line with the concordia marks the*  
 289 *corrected  $^{238}\text{U}/^{206}\text{Pb}$  and  $^{207}\text{Pb}/^{206}\text{Pb}$ , which are used to calculate the  $^{207}\text{Pb}$ -corrected date. The Stacey-Kramers distance*  
 290 *defines concordance as the distance along the discordia between the upper and lower intersections of the discordia with the*  
 291 *concordia (Equation (14)). (B) The Aitchison distance calculates the Euclidean distance between the analysis and concordia*  
 292 *curve in log-ratio space, where higher distance values are considered more discordant. Figure modified from Vermeesch*  
 293 *(2021).*

### 295 3. Geologic Context

296 Anatolia is composed of a series of subduction complexes, island arcs, and continental terranes that accreted and  
 297 collided from the Late Paleozoic through Cenozoic during the progressive opening and closing of Paleotethys and Neotethys  
 298 seaways (Şengör and Yilmaz, 1981). Today, northwestern Anatolia comprises, from structurally highest (north) to lowest  
 299 (south), the continental Pontides, including the Cretaceous–Eocene forearc-to-foreland Central Sakarya and Sarıcakaya Basins,  
 300 the Permian–Triassic Karakaya Complex, the İzmir-Ankara-Erzincan suture zone and associated Neotethys ophiolites and  
 301 mélangé, and the lower plate Anatolide-Tauride continental terranes (Figure 2). The Pontides basement contains Paleozoic  
 302 paragneiss, schist, and amphibolite rocks intruded by Carboniferous granitoids emplaced during the Variscan orogeny  
 303 (Göncüoğlu et al., 2000; Ustaömer et al., 2012). The nature of the Karakaya Complex is debated but is generally considered a  
 304 subduction-accretion complex associated with the Late Paleozoic–Early Mesozoic closure of the Paleotethys along the  
 305 southern margin of Eurasia (Pickett and Robertson, 1996; Okay and Göncüoğlu, 2004; Federici et al., 2010; Ustaömer et al.,

2016). The Karakaya Complex contains metamafic and metasedimentary rocks interpreted as seamounts of intra-oceanic basaltic composition and forearc basin and trench deposits (Pickett and Robertson, 1996) that were subsequently metamorphosed to blueschist and epidote-amphibolite with minor eclogite facies with estimated temperatures of 340–550 ± 50 °C (Okay et al., 2002; Federici et al., 2010) with phengite, glaucophane, and barrosite Ar-Ar cooling dates around 200–215 Ma (Okay et al., 2002). The youngest Karakaya Complex units are unmetamorphosed or metamorphosed to zeolite to lower greenschist facies (120–376 °C) (Federici et al., 2010) and are unconformably overlain by Jurassic platform carbonates. The Cretaceous to present closure of the Neotethys and associated suturing is recorded in the Central Sakarya and Sarıcakaya Basins located north of the suture zone. Stratigraphic and paleocurrent (Oçakoğlu et al., 2018), provenance (Mueller et al., 2022; Campbell et al., 2023), and mudstone geochemistry records (Açıkalin et al., 2016) show the input of suture zone derived material into the Central Sakarya Basin from the Late Cretaceous through Eocene, interpreted as progressive suture zone uplift and exhumation during ~~accretion and~~ continental collision (Oçakoğlu et al., 2018; Okay et al., 2020; Mueller et al., 2022; Campbell et al., 2023). Cretaceous subduction-related arc volcanism and Paleogene syn-collisional volcanic centers are located within and to the north of the basins (Kasapoğlu et al., 2016; Ersoy et al., 2017, 2023; Keskin and Tüysüz, 2018). By Eocene times, continued collision increased plate coupling which manifested as increased contractional deformation that ~~activated/partitioned the southern Central Sakarya Basin into the Sarıcakaya Basin along~~ the basement-involved Tuzaklı-Gümele Thrust (also termed the Söğüt Thrust or Nallıhan Thrust) (Mueller et al., 2022) ~~and partitioned the southern Central Sakarya Basin into the Sarıcakaya Basin~~. The Eocene Sarıcakaya Basin received sediment from the suture zone and Karakaya Complex to the south and basement-involved thrust sheets to the north (Mueller et al., 2019).



324

325

326

327

Figure 2: (A) Simplified terrane map of Anatolia and (B) geologic map of the Central Sakarya Basin and Sarıcakaya Basin region (after Aksay et al., 2002). (C) Simplified stratigraphic correlation chart and schematic sample distribution. Stratigraphy after Ocakoğlu et al. (2018).

## 328 4 Methods

### 329 4.1 Sample Information

330 Sedimentary rock samples were collected from Upper Cretaceous to Eocene siliciclastic sections in the Central  
331 Sakarya Basin and Sarıcakaya Basin in western Anatolia (Figure 2; Table S1). Detrital zircon U-Pb ages and Hf isotopes from  
332 these samples are already published (cf. Section 8; Mueller et al., 2019, 2022; Campbell et al., 2023); a set of 20 samples were  
333 chosen for detrital rutile U-Pb ~~dating~~ and trace element ~~analyses~~. Heavy minerals were extracted using standard heavy mineral  
334 techniques, including crushing, water table, heavy liquid, and magnetic separation (see supporting information). Rutile grains  
335 were handpicked from the  $\geq 0.3$  amp. magnetic fraction using a Leica M205C binocular microscope. Three samples—  
336 16SKY26, 16SKY42 and 17OZK05—yielded hundreds of rutile grains and we handpicked 260–320 rutile grains from each  
337 sample, ~~whereas all grains were picked from;~~ ~~for~~ samples with smaller yield, ~~all grains were picked~~. The low yield of rutile  
338 grains partially contributes to the low-*n* date distributions of the individual samples. Rutile grains were mounted in epoxy and  
339 polished to expose the internal structure. Rutile mounts were carbon coated and imaged with a TFS Apreo-S with Lovac SEM  
340 with an energy-dispersive detector (EDS) to distinguish TiO<sub>2</sub> grains from other heavy minerals (Figure S1).

### 341 4.2 U-Pb Analytical Protocol

342 Detrital rutile U-Pb geochronology was conducted at the Isotope Geochemistry Lab at the University of Kansas (KU-  
343 IGL) using a Thermo Element2 magnetic sector field ICP-MS coupled to a Photon Machines AnalyteG2 excimer laser ablation  
344 system. The protocol was modified from Rösel et al. (2019) to optimize for low U contents (Text S1; Table S2). The ICP-MS  
345 was manually tuned using NIST SRM 612 reference material glass to optimize for high sensitivity and low oxide production.  
346 Grains were ablated for 25 seconds with a laser beam diameter of 50  $\mu\text{m}$ , laser fluence of 3.0 J/cm<sup>2</sup>, and 10 Hz repetition rate.  
347 The U-Pb data were collected in 4 analytical sessions. The analytical protocol was modified from session to session to optimize  
348 for the analysis of low U and Pb unknowns and high U and Pb reference materials. In the first two analytical sessions, 21RtF  
349 and 21RtG, Pb and Th isotopes were measured with the secondary electron multiplier operating in counting detection mode,  
350 whereas Pb and Th isotopes were measured with the secondary electron multiplier in both counting and analog modes ('both  
351 mode') for the final two sessions, 21RtA and 21RtB. Primary and secondary reference materials were the R10 ( $1091.6 \pm 3.5$   
352 Ma by TIMS, 2s abs.; Luvizotto et al., 2009), Wodgina ( $2845.8 \pm 7.8$  Ma by TIMS; Ewing, 2011), 9826J ( $381.9 \pm 1.1$  Ma by  
353 TIMS; Kylander-Clark, 2008), LJ04-08 ( $498 \pm 3$  Ma by LA-ICP-MS; Apen et al., 2020), and Kragerø ( $1085.7 \pm 7.9$  Ma by  
354 TIMS; Kellett et al., 2018). For U-Pb analyses, the analysis of 5-8 unknowns was followed by 2 standards, the primary standard  
355 R10 and one of the secondary standards. The data were reduced in iolite 4 (Paton et al., 2011), calibrated against R10  
356 uncorrected for initial Pb, and using the weighted linear fit drift correction which reproduced secondary standard ages and  
357 brought their MSWDs closest to 1. The concordia ages are satisfactory for all reference materials, except for the Wodgina and  
358 Kragerø, which did not perform well during the first two analytical sessions—likely due to <sup>206</sup>Pb counts per second exceeding  
359 the limit of linear behavior in counting detection mode—and are discarded from those analytical sessions. Standard

360 reproducibility is discussed further in the supplemental text included in the data repository; U-Pb data are provided in the data  
361 repository (Mueller et al., 2023).

### 362 4.3 Trace Element Geochemistry Analytical Protocol

363 Detrital rutile trace element geochemistry ( $^{49}\text{Ti}$ ,  $^{51}\text{V}$ ,  $^{53}\text{Cr}$ ,  $^{66}\text{Zn}$ ,  $^{69}\text{Ga}$ ,  $^{90}\text{Zr}$ ,  $^{93}\text{Nb}$ ,  $^{95}\text{Mo}$ ,  $^{118}\text{Sn}$ ,  $^{121}\text{Sb}$ ,  $^{177}\text{Hf}$ ,  $^{181}\text{Ta}$ ,  $^{182}\text{W}$ )  
364 was conducted at the KU-IGL using the same instrumentation and parameters, except with a 25 or 35  $\mu\text{m}$  spot size. Reference  
365 materials included USGS GSD-1G and USGS GSC-1G glasses (Jochum et al., 2011) and R10 rutile (Luvizotto et al., 2009).  
366 For trace element analysis, the analysis of 5–10 unknowns was followed by analysis of 2 standards, the primary standard GSD-  
367 1G and one of the secondary standards. Trace element concentrations were calculated using the Trace Element routine in iolite  
368 4 with  $^{49}\text{Ti}$  as an internal standard; for rutile unknowns,  $\text{TiO}_2$  was set to be 100 mass-% (e.g., Plavsa et al., 2018; Rösel et al.,  
369 2019). Standard reproducibility is discussed in the supporting information in the data repository (Text S2). In short, for the  
370 secondary standard GSC-1G, all elements are within 10% of the published values except for Sn and Ga, and for the secondary  
371 standard R10, all results are within the range of reported values. Following U-Pb and trace element analysis, mounts were  
372 imaged in an SEM at University of Nevada Reno (Figure 3). Most grains have both U-Pb and trace element results, but some  
373 grains have only U-Pb results due to the grains being too small for a second ablation spot or only trace element results due to  
374 discarded U-Pb data. Detrital rutile trace element data are given in the data repository (Mueller et al., 2023).

### 375 4.4 Additional Data Workflows

376 Additional data reduction and data calculations steps were performed. Provided as a complement to this manuscript  
377 are open access Jupyter Notebooks that contain the Python and R code used to perform these additional calculations and to  
378 generate figures, which are briefly described here (Mueller, 2024). (1) The  $^{208}\text{Pb}$  and  $^{207}\text{Pb}$  corrections were performed in the  
379 Detrital-Common-Pb-Corrections notebook using the equations detailed in Section 2 above. The notebook allows for either a  
380 manually set number of iterations or to iterate until all analyses are below a given threshold—the percent difference in corrected  
381 date between the current and previous iteration. Presented here are the results from the 200<sup>th</sup> iteration. (2) The UPb-Plotter  
382 notebook visualizes the uncorrected U-Pb results in Tera-Wasserburg space, compares metrics for excluding analyses based  
383 on uncertainty filters (Section 5.3), and calculates discordance using the Stacey-Kramers and Aitchison distances (Section 2;  
384 [Text S3; Figures S7-S8](#)). (3) The Rutile-Trace-Elements notebook includes the calculations and resulting figures for  
385 exploring  $\text{TiO}_2$  polymorphs, mafic and pelitic protoliths, Zr-in-rutile thermometry, and low U contents. [Discrimination](#)  
386 [diagrams using V, Cr, Zr, Fe, and Nb](#) ~~Here, rutile distinguish rutile from other  $\text{TiO}_2$  polymorphs (Triebold et al., 2011), and all~~  
387 [analyzed grains plot within the rutile field \(Figure S2\)](#). Rutile grains are classified as mafic or pelitic based on the Cr-Nb  
388 discrimination fields of Triebold et al. (2012), and Zr-in-rutile temperatures are calculated with the Kohn (2020) formulation  
389 (Equation (1)) at 13 kbar. (4) The Detrital-PCA-R notebook performs principal component analysis on trace element data using  
390 the pcaCoDa function in the robCompositions library, which is designed to handle compositional data (Templ et al., 2011).  
391 ~~(5) Due to the variable performance of Sn and Ga in the secondary standards, these elements were excluded from the PCA~~

392 ~~(Supplemental Text S2, Figure S6). Additionally, Mo and Sb were excluded because grains with very low or zero~~  
393 ~~concentrations influence the results to be artificially dominated by these elements. (5) Additionally, the UPb-Timeseries~~  
394 notebook is provided for visualizing U-Pb timeseries data.

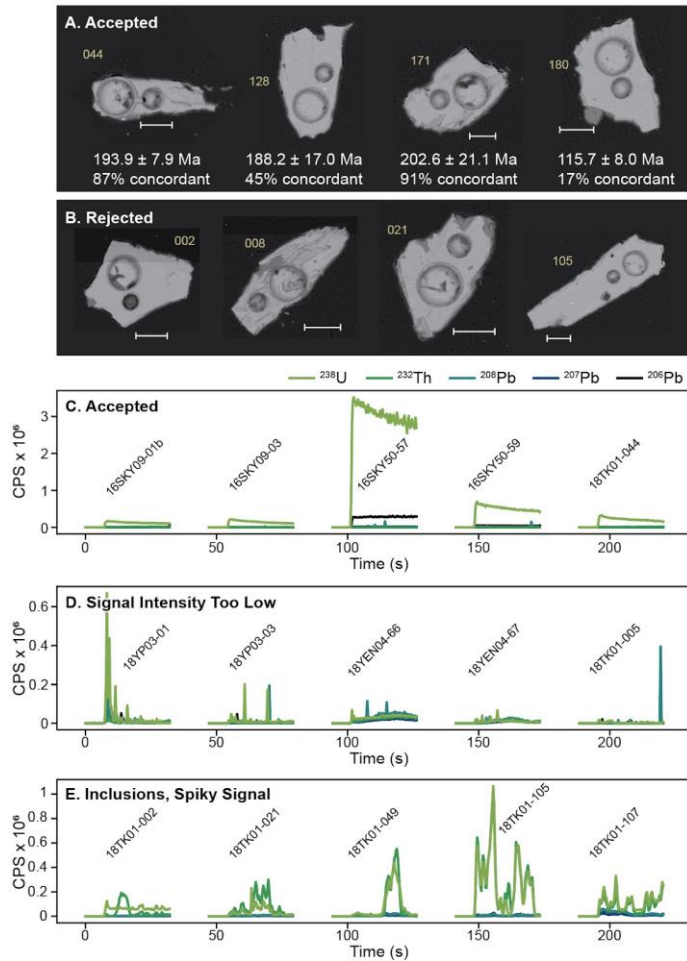
## 395 **5 U-Pb Geochronology Results**

### 396 **5.1 U-Pb Data Quality**

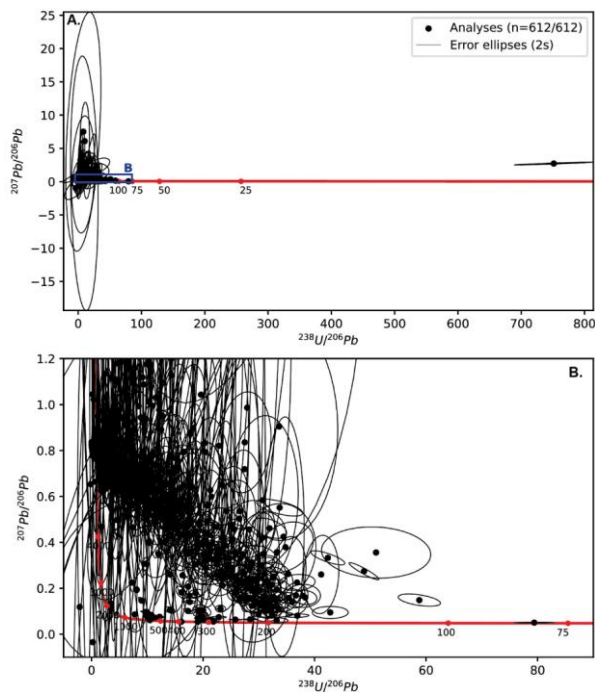
397 A total of 1,278 detrital rutile grains were analyzed for U-Pb geochronology. A significant number of analyses were  
398 rejected and excluded, as discussed below. We aim to be transparent in data reporting—including the number of grains  
399 analyzed and the criteria for rejection—in order to give precedence for this practice, which is missing in the literature, and to  
400 explore the current limitations of large-*n* detrital rutile studies. Even with the optimized LA-ICP-MS protocol, a significant  
401 number of analyses did not meet quality control goals: 665 of 1,277 (54%) analyses were rejected due to anomalous (spiky)  
402 patterns in raw signal intensity, or low U or low Pb signal intensity. Figure 3 depicts representative examples of signal intensity  
403 in accepted and rejected analyses. Inclusions and anomalous patterns were easily spotted through monitoring  $^{206}\text{Pb}$ ,  $^{207}\text{Pb}$ ,  $^{238}\text{U}$ ,  
404  $^{232}\text{Th}$ ,  $^{206}\text{Pb}/^{238}\text{U}$  and  $^{207}\text{Pb}/^{206}\text{Pb}$  channels. In some instances, the signal of an inclusion or anomalous (spiky) pattern was short  
405 enough that the integration window could be shortened to exclude it. In other cases, the non-inclusion signal could not be  
406 isolated and the entire analysis was discarded. Potential causes for the abnormal signal patterns and high Pb uncertainty include  
407 (1) elemental heterogeneity from ablating into small inclusions and/or lamellae; (2) inhomogeneities due to micro-cracks with  
408 different element/isotope composition; (3) heterogeneous amount of common lead incorporation during rutile growth; (4)  
409 textural and/or elemental heterogeneities due to multiple rutile growth events. Although, scenarios 3 and 4 are unlikely for Pb  
410 because it diffuses and should not cause spikes.

411 The SEM images do not give a clear picture of how to better select grains that will produce acceptable signal intensity  
412 and U-Pb concordance. Figure 3 shows SEM images of representative rutile grains after laser ablation. All grains appeared  
413 inclusion-free before ablation, yet some analyses clearly ablated into inclusions (Figure 3b,e). The large laser spot size of 50  
414  $\mu\text{m}$  gives a higher signal, which is better for grains with potentially low U or low Pb concentrations, but the potential trade-off  
415 is increasing the likelihood of hitting inclusions. Grains with obvious inclusion lamellae generally yielded poor data quality.





416 *Figure 3: SEM BSE images and U-Pb signal intensities of representative rutile grains. (A) Rutile grains with acceptable U-*  
 417 *Pb analyses across a range of concordance. U-Pb date and concordance are from the <sup>207</sup>Pb correction method and Stacey-*  
 418 *Kramers metric, respectively. Ablation pits are from U-Pb analysis (larger) and trace element analysis (smaller). The scale*  
 419 *bar is 50 μm. All grains are from sample 18TK01; the grain number is in yellow. (B) Images of rutile grains with U-Pb analyses*  
 420 *rejected because of inclusions (18TK01-002) or spiky signal (18TK01-008, -021, -105). (C-E) Representative U-Pb raw signal*  
 421 *intensity patterns of accepted analyses (C) and rejected analyses from too low signal intensity (D) or inclusions and/or spiky*  
 422 *signal (E).*



423

424 *Figure 4. Uncorrected detrital rutile U-Pb results displayed in Tera-Wasserburg space. Uncertainty ellipses are 2s*  
 425 *propagated. The area displayed in (B) is highlighted by the blue box in (A).*

## 426 5.2 U-Pb Geochronology and Common Pb Correction Results

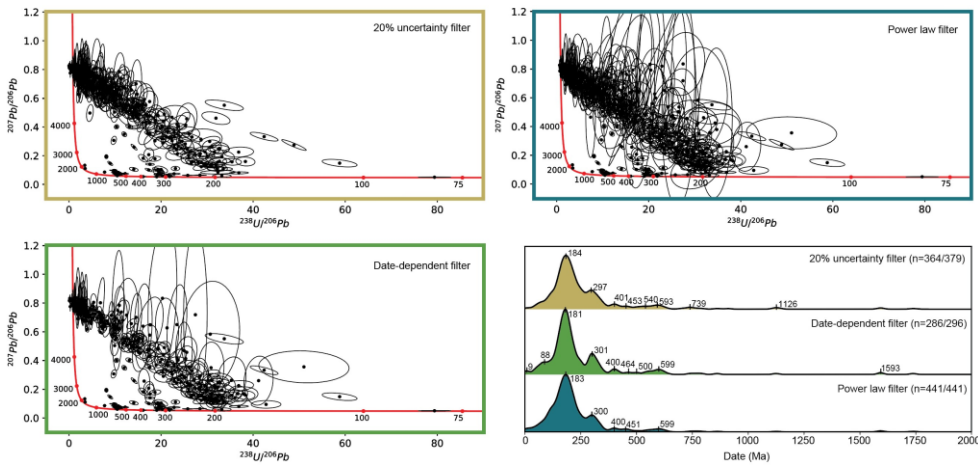
427 The uncorrected U-Pb results are displayed in Figure 4. We note that all concordia diagram figures display the  
 428 uncorrected U-Pb data; common Pb corrections force concordance and the corrected data are displayed as date distributions.  
 429 A number of analyses plot close to the concordia curve and many plot along the discordia trend toward common Pb values.  
 430 Both  $^{208}\text{Pb}$ - and  $^{207}\text{Pb}$ -corrections were performed on the uncorrected U-Pb analyses. After 200 iterations, the  $^{208}\text{Pb}$ - and  $^{207}\text{Pb}$ -  
 431 corrections resulted in 547 and 487 corrected dates between 0 Ma and 4500 Ma, respectively. These numbers differ because  
 432 no corrected date is calculated when the proportion of  $^{206}\text{Pb}_{\text{common}}$  is greater than 1, and because the common Pb corrections  
 433 can yield dates younger than 0 Ma or significantly older than 4500 Ma depending on the calculated proportion of  $^{206}\text{Pb}_{\text{common}}$   
 434 ( $f_{206}$ ). The Pb corrected U-Pb data are shown in Figure 5 as kernel density estimates (KDEs) and cumulative KDE-distributions.



447 **5.3 Uncertainty and Discordance Thresholds**

448 Detrital U-Pb data can further be filtered by U-Pb ratio uncertainty, date uncertainty, or discordance thresholds.  
 449 Because the uncertainty on the corrected date is calculated from the uncertainty on the measured  $^{206}\text{Pb}/^{238}\text{U}$  ratio (cf. Section  
 450 2), these metrics are similar. Figure 6 displays the results of three uncertainty threshold filters: (1) 20% uncertainty on  
 451  $^{238}\text{U}/^{206}\text{Pb}$  and  $^{207}\text{Pb}/^{206}\text{Pb}$  ratios (modified from Lippert, 2014), (2) a date-dependent filter that excludes analyses with > 10%  
 452 date uncertainty for corrected dates > 100 Ma, > 20% uncertainty for dates 10–100 Ma, or > 25% uncertainty for dates < 10  
 453 Ma (after Govin et al., 2018), and (3) a power law threshold that excludes analyses if the percent uncertainty on the  $^{207}\text{Pb}$   
 454 corrected date exceeds the function:  $(t \wedge -0.65) * 8$  (after Chew et al., 2020). The results of these filters are displayed as  
 455 uncorrected U-Pb data in Tera-Wasserburg space and  $^{207}\text{Pb}$  corrected date distributions (Figure 6). From the total  $^{207}\text{Pb}$   
 456 corrected analyses total (n=487), the above thresholds exclude an additional 108 (22%), 191 (39%), and 46 (9%) analyses,  
 457 respectively. The power law function excludes the fewest number of analyses.

458 The three filters have similar  $^{207}\text{Pb}$  corrected date distributions (Figure 6). The main age modes identified in all three  
 459 filters are 183 Ma, 300 Ma and 400 Ma. Minor Devonian and older date modes are present. Only the date-dependent filter  
 460 identifies the 89 Ma date mode and it includes a 9 Ma mode that is significantly younger than the youngest sampled strata  
 461 (Bartonian–Priabonian). The U-Pb ratio uncertainty and power law filters have nearly identical date peaks with the power law  
 462 filter including more grains, especially in the ~183 Ma mode.  
 463



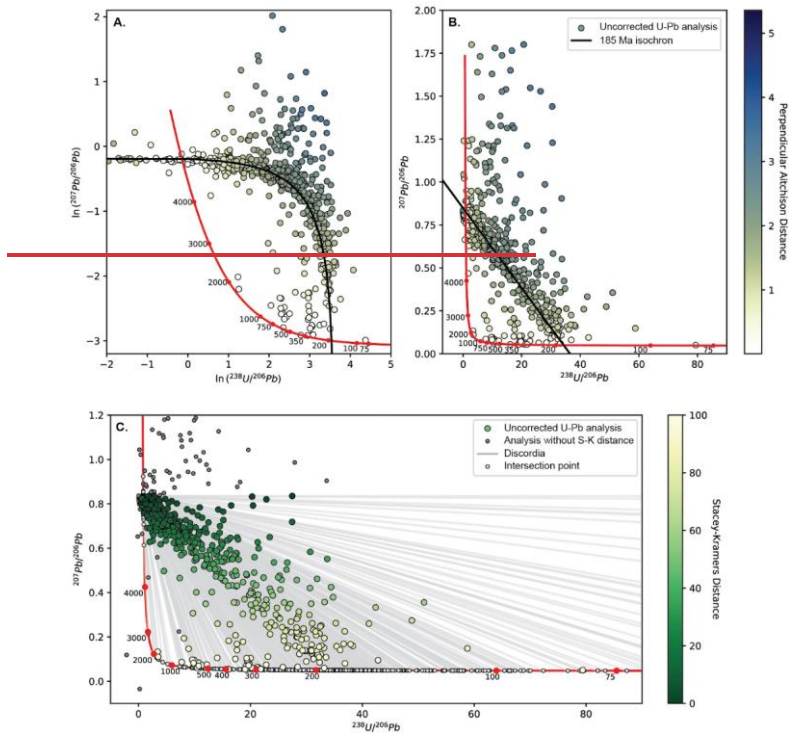
464  
 465 *Figure 6. Comparison of U-Pb filters based on U-Pb ratio and date uncertainties, displayed in Tera-Wasserburg space*  
 466 *(uncorrected) and normalized kernel density estimates ( $^{207}\text{Pb}$ -corrected). The U-Pb ratio uncertainty filter (yellow) excludes*  
 467 *all analyses with  $^{238}\text{U}/^{206}\text{Pb}$  and  $^{207}\text{Pb}/^{206}\text{Pb}$  ratio uncertainties above 20% (modified from Lippert, 2014). The date-dependent*

468 filter (green) excludes analyses based on the  $^{207}\text{Pb}$ -corrected date and uncertainty (see text; after Govin et al., 2018); after  
469 Govin et al., 2018). The power law filter (blue) excludes analyses if the percent uncertainty on the  $^{207}\text{Pb}$  corrected date exceeds  
470 the given power law function (see text; after Chew et al., 2020).

471

472 ~~The Stacey-Kramers distance is used to~~ quantify discordance in common Pb bearing minerals. ~~two metrics are~~  
473 ~~considered: Aitchison and Stacey-Kramers distances (1 (Text S3; Figure S7)).~~ The results are shown in ~~7~~Figure S8 in Tera-  
474 Wasserburg space with uncorrected U-Pb analyses colored by distance (concordance). In the Stacey-Kramers distance  
475 formulation, The Aitchison distance is calculated as the Euclidean distance between the analysis and concordia curve in log-  
476 ratio space, where higher distance values are considered more discordant. The results show that analyses closest to concordia  
477 are the least discordant (most concordant). This means that analyses close to the lower concordia curve and the common Pb  
478 composition are considered less discordant (more concordant) whereas analyses in the middle space are considered most  
479 discordant (7b). ~~In the Stacey-Kramers distance formulation, discordance is calculated from the distance between the analysis~~  
480 ~~and the upper and lower intercepts (Equation (14)). In this case, analyses closest to the common Pb composition are considered~~  
481 ~~most discordant (7most discordant (Figures S7 and S8).e).~~ ~~If a discordance filter were applied based on the Aitchison distance,~~  
482 ~~analyses in the middle space of the concordia diagram would be excluded, whereas a discordance filter based on the Stacey-~~  
483 ~~Kramers distance would exclude analyses closer to the common Pb composition.~~ The Stacey-Kramers distance appears to  
484 reflect U-Pb systematics in common Pb bearing minerals and is a representative metric of discordance.

485



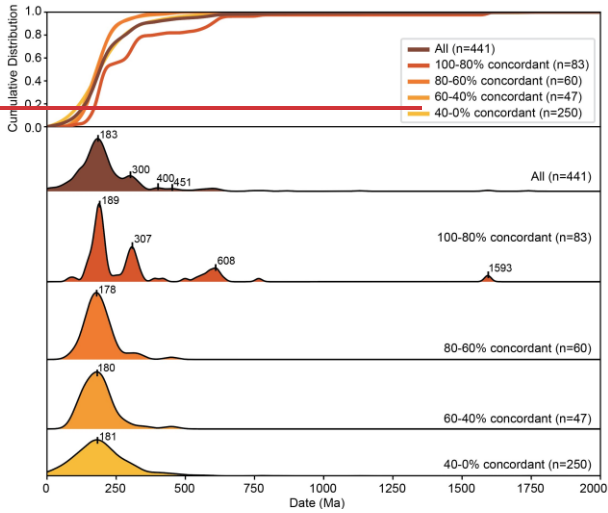
486  
 487 *Figure 7. Comparison of (A,B) Aitchison distance and (C) Stacey-Kramers distance as metrics for discordance in common Pb*  
 488 *bearing minerals. For simplicity all uncorrected U-Pb data are shown as circles rather than error ellipses. Circles are color-*  
 489 *coded by distance (concordance). The Aitchison distance results are shown in Tera-Wasserburg concordia diagrams in*  
 490 *original (B) and log-ratio space (A). The 185 Ma isochron is displayed in both diagrams. Circles closest to the concordia have*  
 491 *the lowest discordance (highest concordance). (C) The Stacey-Kramers distance results are shown in Tera-Wasserburg space,*  
 492 *where the gray lines are individual discordia and light gray circles are intersection points. Uncorrected U-Pb circles are*  
 493 *color-coded for percent distance along the total discordia distance (from common Pb composition to lower intersection point).*  
 494 *Circles closest to the lower concordia intercept have the lowest discordance. Dark gray circles are U-Pb analyses without*  
 495 *Stacey-Kramers distance values (no lower intersection point due to positive discordia line slope, for example) or without <sup>207</sup>Pb-*  
 496 *corrected dates (due to  $f_{206} > 1$ ).*

497  
 498 The U-Pb dates are subdivided into bins based on their Stacey-Kramers concordance values. Figure 8 displays the <sup>207</sup>Pb-  
 499 corrected date distributions filtered using the power law threshold and subdivided into bins based on their Stacey-Kramers  
 500 concordance values. The 100-80% concordance group has the most discrete date modes at 189 Ma, 307 Ma, 608 Ma, and  
 501 1593 Ma. The 80-60%, 60-40% and 40-0% bins have unimodal age distributions that are asymmetric toward older dates, and

Formatted: Indent: First line: 0"

502 have a dominant age mode around 180 Ma. The cumulative distributions reveal that the distribution of all grains together has  
 503 a similar distribution to that of the 40-0% group (Figure 8 top). Comparison of the whole distribution of all grains together  
 504 to the 100-80% concordance group reveals that, if a 20% discordance filter were applied similar to detrital zircon U-Pb  
 505 workflows, the same general date modes would be identified. However, the addition of lower concordance grains (i.e., 80-0%  
 506 concordance groups) broadens the Jurassic peak and shifts it slightly younger from 189 Ma to ~180 Ma, decreases the  
 507 amplitude of the Carboniferous and Proterozoic peaks, and increases the amplitude of the ~400-450 Ma peaks.

508



509

Formatted: Justified

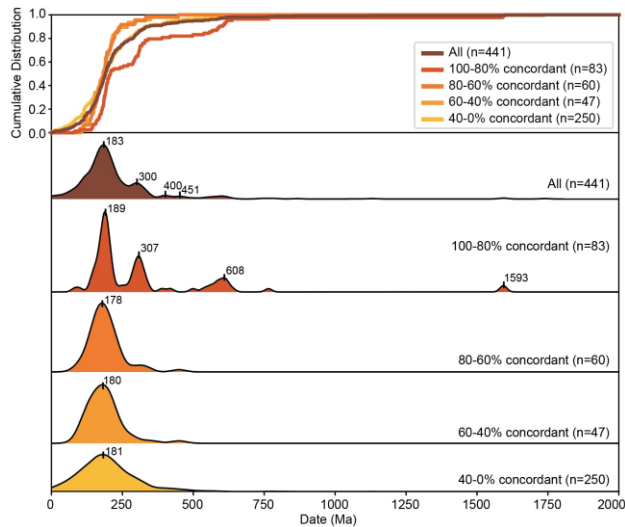


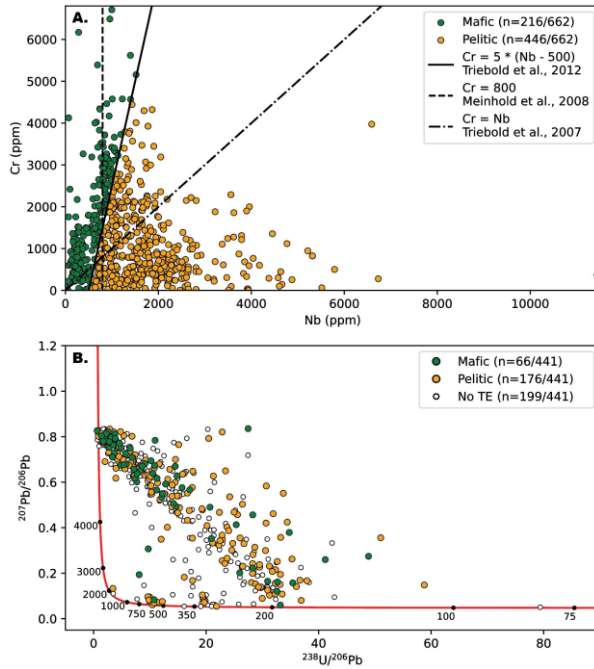
Figure 8. Relative kernel density estimates (KDEs; bottom panels) and cumulative KDE distributions (top) of  $^{207}\text{Pb}$ -corrected, power law uncertainty filtered dates categorized by discordance from Stacey-Kramers distance values.

## 6 Trace Element Geochemistry Results

### 6.1 Metamorphic Protolith

Trace element results are provided in the data repository. Discrimination diagrams using V, Cr, Zr, Fe, and Nb can distinguish rutile from other  $\text{TiO}_2$  polymorphs (Triebold et al., 2011), and all analyzed grains plot within the rutile field (Figure S2). The Cr and Nb concentrations discriminate between metapelitic and metamafic source rocks (Zack et al., 2004a; Triebold et al., 2011, 2012). Even though there are multiple proposed discrimination lines between metamafic and metapelitic source lithologies (e.g., Meinhold et al., 2008; Triebold et al., 2012), the detrital rutile in this dataset plot in both the metamafic (33%) and metapelitic (67%) fields (Figure 9a). There is no clustering of protolith by U-Pb date, with prominent date modes containing both metamafic and metapelitic grains (Figure 9b). While some metamafic grains plot close to concordia (more concordant), many plot close to the common Pb composition concordia intercept (more discordant).





523

524 Figure 9. (A) Protolith discrimination diagram. Grains are classified as (meta)mafic and (meta)pelitic based on the Triebold  
 525 et al. (2012) line, with the Triebold et al. (2007) and Meinhold et al. (2008) lines also shown. (B) Concordia diagram of  
 526 uncorrected U-Pb circles colored by protolith classification. The power law filter is applied. Open circles represent grains  
 527 with U-Pb data but no trace element data (TE). Sample size differs between plots because not all grains have both U-Pb and  
 528 trace element data.

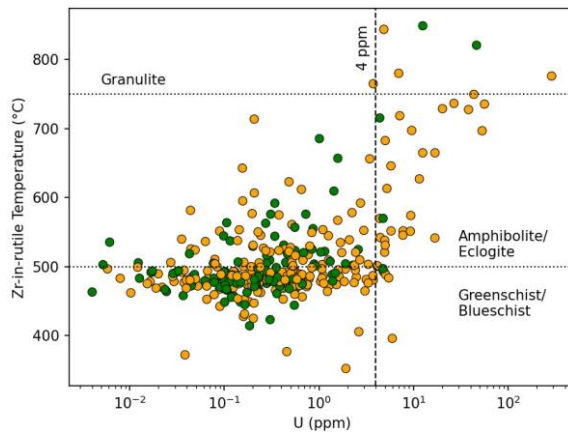
## 529 6.2 Zr-in-Rutile Temperature and Uranium Concentration

530 The Zr-in-rutile temperatures were calculated using the Kohn (2020) calibration (Equation (1)) at 13 kbar with an  
 531 uncertainty of 5 kbar; results are included in the data repository. The Zr concentrations range from 2 to 1934 ppm, yielding  
 532 source rock minimum peak temperatures from  $336 \pm 15$  °C to  $849 \pm 28$  °C. The Zr-in-rutile temperature results are displayed  
 533 alongside U concentration and colored by protolith (Figure 10). There is not a correlation between Zr-in-rutile temperature and  
 534 protolith. The majority of grains have moderate temperatures corresponding to greenschist to blueschist facies conditions: 68%  
 535 (n=147/216) of mafic and 67% (n=301/446) of pelitic grains are below 500 °C. There are fairly consistent Zr-in-rutile  
 536 temperatures within theWhen displayed in Tera-Wasserburg space, dominant date modes—90 Ma, 185 Ma, 300 Ma, 500–650  
 537 Ma—have fairly consistent Zr-in-rutile temperatures (Figure 11 ()). The highest temperatures, reaching granulite facies

538 conditions, are found in the 90 Ma date mode. The 500–650 Ma and 300 Ma rutile grains similarly preserve high temperatures,  
539 up to 700–820 °C, whereas the majority of 185 Ma grains have temperatures in greenschist to blueschist facies around 450–  
540 550 °C.

541 The uranium concentrations range from 0.00206 to 113 ppm. These low values are **abovewithin** the detection limit.  
542 The primary standard, R10, has a U concentration of 44 ppm (Luvizotto et al., 2009) and, in our measurements, on average, 2.1  
543 million CPS  $^{238}\text{U}$  (i.e., ~50,000 counts/ppm). The  $^{238}\text{U}$  baseline was about 5 CPS, therefore, the instrument set-up has a  
544 detection limit of about 0.0003 ppm  $^{238}\text{U}$  (calculated from 3x background). All analyses are above the detection limit, with  
545 91% (n=555/612) of analyses at least an order of magnitude above this limit. The comparison of Zr-in-rutile temperatures with  
546 U concentration reveals that the majority of low U rutile (< 4 ppm) are within greenschist to blueschist facies conditions (68%,  
547 n=205/303 below 500 °C; Figure 10). Additionally, mafic classified grains are dominantly low U (95%, n=106/112 below 4  
548 ppm). The majority of rutile with U contents above 4 ppm are classified as pelitic (85%, n=34/40) and generally have higher  
549 Zr contents.

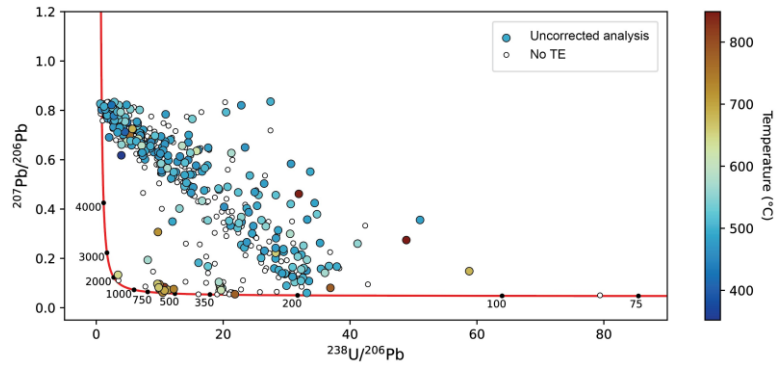
550



551

552 *Figure 10. Zr-in-rutile temperature versus U concentration. Mafic and pelitic discrimination is from Cr and Nb concentrations*  
553 *(Figure 9) mafic protoliths shown in green, pelitic in orange. The 4 ppm U line demarcates grains included/excluded by a U*  
554 *filter. Zr-in-rutile temperatures follow the Kohn (2020) calibration. Note that not all analyses have both U and trace element*  
555 *(TE) data, therefore there are fewer grains represented in this scatter plot than in Figure 9.*

556



557

558 *Figure 11. Uncorrected rutile U-Pb results in Tera-Wasserburg space colored by Zr-in-rutile temperature calculated from the*  
 559 *Kohn (2020) calibration. The mode centered around 95 Ma has the highest temperatures, and modes centered around 300 Ma*  
 560 *and 500–650 Ma also contain high temperatures, whereas the 185 Ma mode is predominantly composed of moderate*  
 561 *temperature grains. Open circles are rutile U-Pb analyses without trace element (TE) data. Colormap is from Crameri (2020).*

562

### 6.3 Principal Component Analysis

563

564

565

566

567

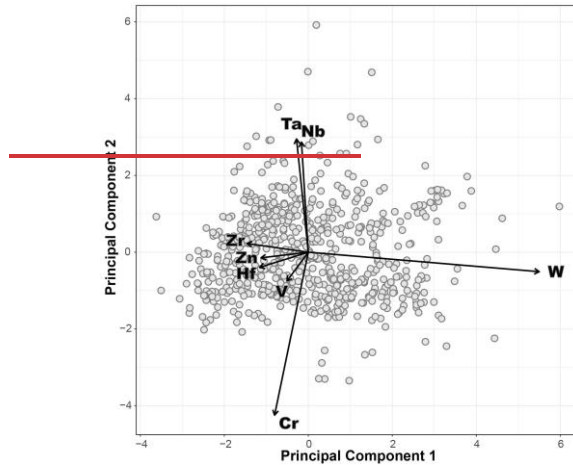
568

569

570

571

Principal component analysis (PCA) was conducted on the detrital rutile trace element compositions (V, Cr, Zn, Zr, Nb, Hf, Ta, W) using an in-house R code (cf. Section 4.4; Mueller, 2024) and the results are given in the data repository. PCA is a multivariate statistical procedure that identifies the variables that explain the most amount of variance within a dataset. The principal components are ranked based on the amount of variance they explain. Plots of principal component ‘loadings’ display the distribution of the trace element variables with respect to the principal components. The scores and loadings in 12 show that the variance between rutile grains can largely be explained by Cr, Nb and Ta, and W, Zr, and Hf. Because Cr, Nb and Ta are protolith dependent (PC 2) and Hf and Zr are temperature dependent (PC 1), the variance in detrital rutile trace element chemistry is best explained by both protolith and metamorphic grade, tracking these two properties of source rocks. The protolith and temperature components capture the most important portion of the trace element results.



572  
573 *Figure 12.-PCA score and loadings plot of principal components 1 and 2, which cumulatively explain 66.6% of trace element*  
574 *variance. The variance in trace element chemistry is best explained by metamorphic grade (PC 1) and protolith (PC 2).*

575 **7 Discussion**

576 **7.1 Recommendations for U-Pb Data Rejection, Correction, and Filtering**

577 The complex, natural dataset presented here allows an examination of the current practices of data reporting and  
578 limitations of large-*n* detrital rutile studies. In this study, a large number of analyses were rejected during U-Pb data reduction,  
579 but the SEM images do not provide simple criteria (e.g., inclusions, fractures) for how to better select grains that will produce  
580 acceptable signal quality or lower U-Pb discordance (Figure 3). All areas selected for analysis appeared inclusion-free before  
581 ablation, yet some analyses evidently ablated into inclusions (Figure 3b,e). Because we expected grains from mafic sources  
582 with low U or low Pb concentrations, we used a large 50  $\mu\text{m}$  laser beam diameter, but this potentially increased the probability  
583 of hitting inclusions. While rejecting analyses is not ideal, low U and Pb signal intensities are not unexpected in natural  
584 samples, so some degree of data rejection is to be anticipated, especially given the predicted metamafic (very low U) protolith  
585 sources. We contend here that while the exclusion of data from interpretation is common to many detrital rutile studies (e.g.,  
586 Bracciali et al., 2013; Rösel et al., 2014, 2019; Caracciolo et al., 2021), ours included. However, in most studies, the number  
587 of discarded analyses and criteria for discarding analyses during U-Pb data reduction are unclear or not mentioned, thereby  
588 limiting opportunities to evaluate data quality and navigate results in a potentially meaningful way. We recommend that these  
589 criteria be explicitly stated and discussed in all studies using detrital rutile U-Pb geochronology.

Formatted: Font color: Black

590 ~~We reiterate that the number of discarded After U-Pb data reduction, additional analyses is surprising but is the result~~  
591 ~~of a natural dataset were excluded during common Pb correction, and not analytical or data reduction error. Daily instrument~~  
592 ~~tuning on NIST 612 glass produced stable signal, high count rates and low oxide production (Table S2), therefore, the grains~~  
593 ~~rejected due to “spiky” raw signal intensity are not a sign of poor instrument set-up. Further, a comparison of U-Pb precision~~  
594 ~~between our results and other rutile U-Pb studies demonstrates that, for rutile with U concentrations in the parts per million~~  
595 ~~range (> 1 ppm U), we achieve lower uncertainty filtering. Here, the <sup>208</sup>Pb and <sup>207</sup>Pb corrections produce similar date spectra~~  
596 ~~(Figure 5) as do the various uncertainty filters (Figure 6 compared with unknowns analyzed on a multi-collector and similar~~  
597 ~~precision for reference materials analyzed on a Q-ICP-MS. Additionally, this study’s rutile range extends to 100 times or lower~~  
598 ~~uranium concentration than rutile analyzed by other instrument set-ups. Rutile with high uncertainty in this study is in the~~  
599 ~~lower U range (< 1 ppm U).~~

600 ~~The uncorrected U-Pb results include many discordant analyses (). If treated similar to detrital zircon ). We tentatively~~  
601 ~~favor the power-law uncertainty filter as it does not appear to alter the presence or proportion of individual age populations,~~  
602 ~~and because this filter excludes the fewest analyses. Future work is needed to determine if this holds in other datasets. We~~  
603 ~~propose that the Stacey-Kramers distance is a better metric than Aitchison distance for quantifying discordance as it reflects~~  
604 ~~U-Pb systematics (7). A discordance threshold is not recommended as an exclusion criterion based on the similarity of the date~~  
605 ~~distributions across concordance bins (Figure 8, many analyses would be excluded by). Further, most mafic-classified grains~~  
606 ~~plot closer to common Pb compositions, so a discordance filter would bias results toward pelitic and high U grains (Figure 9.~~  
607 ~~However, including). Including initially discordant data is acceptable because geologically meaningful interpretations can be~~  
608 ~~made from initially discordant data when appropriate common Pb corrections are applied. Note that common <sup>208</sup>Pb and <sup>207</sup>Pb~~  
609 ~~corrections force concordance so that initially discordant data are concordant after correction. U-Pb discordance in common~~  
610 ~~Pb bearing minerals is well documented in published reference materials (e.g., Chew et al., 2011, 2014). In petrochronologic~~  
611 ~~applications, *in-situ* work demonstrates that individual analyses can be nearly 100% discordant and still interpreted confidently~~  
612 ~~within the population of co-genetic grains (e.g., Poulaki et al., 2023). Although some detrital rutile U-Pb datasets are dominated~~  
613 ~~by concordant analyses (e.g., Rösel et al., 2019, Kooijman et al. 2010), many detrital datasets contain analyses across the~~  
614 ~~concordance spectrum, including highly discordant analyses, whose Pb-corrected dates are used in interpretations (Bracciali~~  
615 ~~et al., 2013; Mark et al., 2016; O’Sullivan et al., 2016; Govin et al., 2018; Ershova et al., 2024). Note that common <sup>208</sup>Pb and~~  
616 ~~<sup>207</sup>Pb corrections force concordance so that initially discordant data are concordant after correction. We propose that the Stacey-~~  
617 ~~Kramers distance is a suitable metric for quantifying discordance as it reflects U-Pb systematics (Figure S8). However, a~~  
618 ~~discordance threshold is not recommended as an exclusion criterion based on the similarity of the date distributions across~~  
619 ~~concordance bins (). Further, most mafic-classified grains plot closer to common Pb compositions, so a discordance filter~~  
620 ~~would bias results toward pelitic and high U grains (). For these reasons, we do not advocate filtering detrital rutile U-Pb data~~  
621 ~~based on discordance.~~

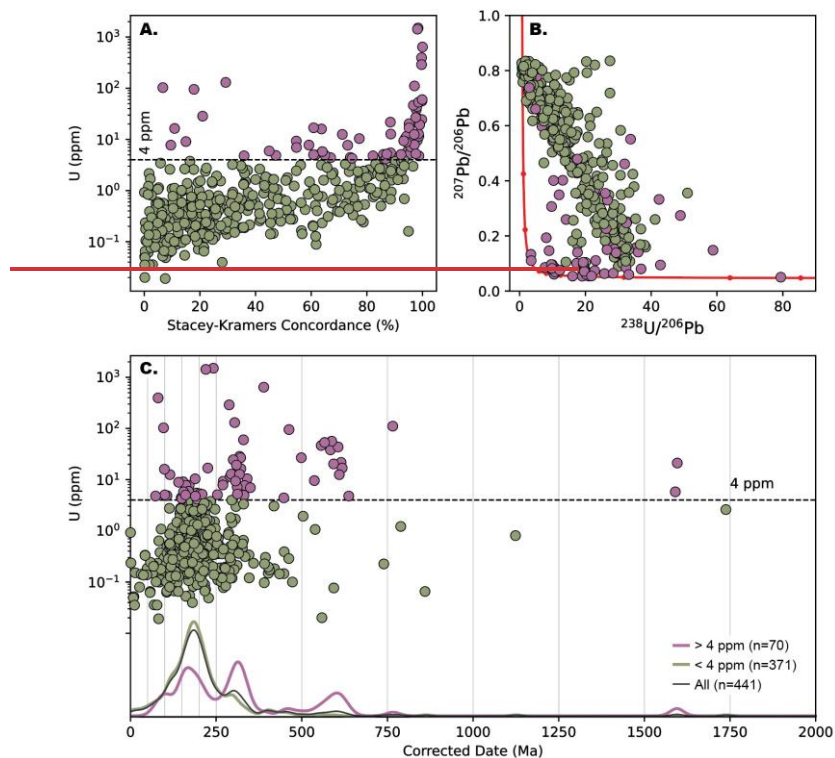
622 ~~After U-Pb data reduction, a common Pb correction and uncertainty filter were applied, which further excluded~~  
623 ~~analyses. In this dataset, the <sup>208</sup>Pb and <sup>207</sup>Pb corrections produce similar date spectra (), and either correction method can be~~

Formatted: Font color: Auto

Formatted: Font color: Auto

624 used. Similarly, the various uncertainty filters produce similar date distributions () and we tentatively favor the power law  
625 uncertainty filter as it does not appear to alter the presence or proportion of individual age populations, and because this filter  
626 excludes the fewest analyses. For these reasons, we do not advocate filtering detrital rutile U-Pb data based on discordance.  
627 Future work with large-*n* detrital datasets is needed to explore ~~how the influence of~~ common Pb corrections, ~~discordance and~~  
628 ~~data filters, and based on~~ uncertainty ~~and discordance, including whether these~~ filters influence date distributions in other  
629 datasets.

630 Expanding detrital rutile U-Pb applications is hindered by data rejection, as seen in this dataset and others. Caracciolo  
631 et al. (2021) attempted to present a large-*n* detrital rutile dataset in which rutile grains were identified via Raman spectroscopy.  
632 Their workflow using automated Raman is better suited for identifying polymorphs and reducing bias than the handpicking  
633 and SEM-EDS workflow used here and in many other studies. However, of the 712 detrital rutile grains analyzed by Caracciolo  
634 et al. (2021), only 347 grains remained (48%) after their data reduction and uncertainty filtering (using a modified power law  
635 filter). Similar to our dataset, there were not enough rutile dates per sample to discuss sample-by-sample provenance  
636 interpretations (Figure S7). Govin et al. (2018) discarded 36% (n=53/146) of detrital rutile U-Pb analyses using their date-  
637 dependent filter. Shaanan et al. (2020) present the only other detrital rutile dataset from Anatolia that does not impose a low-  
638 U filter; they discard 60% (n=97/163) of their data during discordance filtering. Together these studies illustrate that there is a  
639 formidable ~~methodological~~ hurdle in trying to scale up detrital rutile U-Pb to large-*n* provenance applications.



640  
 641 *Figure 13–Comparison of detrital rutile filtering based on U concentration or concordance. (A) Rutile U concentration versus*  
 642 *percent concordance (Stacey-Kramers distance). The U-threshold filter groups grains greater than and less than 4 ppm U. (B)*  
 643 *Rutile U-Pb results in Tera-Wasserburg space following the color scheme in panel A. (C) Rutile U concentration versus*<sup>207</sup>*Pb-*  
 644 *corrected U-Pb date. The relative KDEs display the date spectra from the different U concentration groups: all analyses,*  
 645 *above 4 ppm U, below 4 ppm U. The power-law filter is applied to all plots in the figure.*

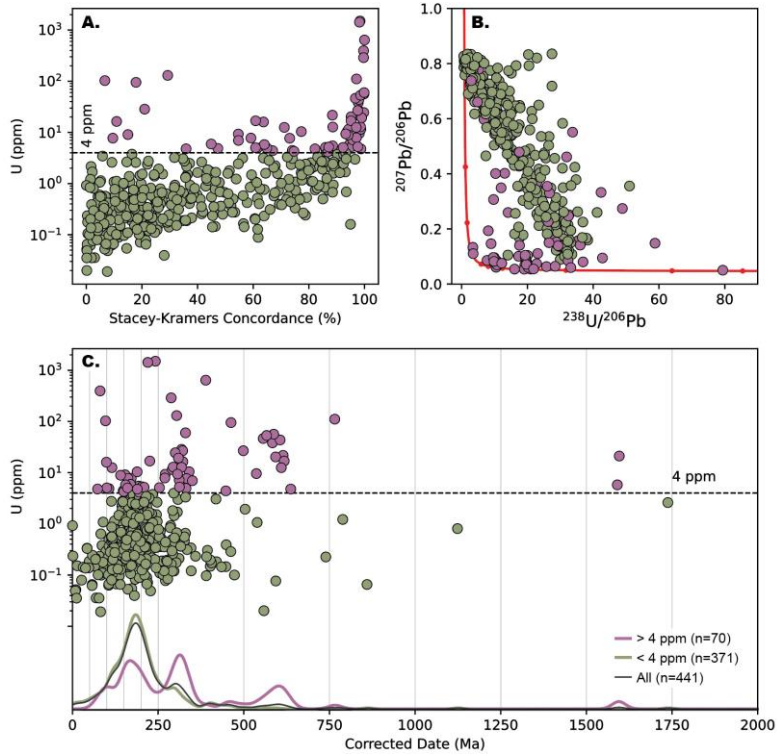
## 646 7.2 Low Uranium Rutile

647 Rejecting and filtering data is a common practice, whether due to abnormal signal intensity pattern, discordance, or  
 648 high uncertainty. A filter based on the raw data (i.e., low U CPS) is directly linked to counting statistics, which is a fundamental  
 649 statistical limitation and not instrument type or instrument setting specific. Figure S12 shows that the main issue with the  
 650 dataset presented here is the very low U and therefore Pb concentration. We demonstrate that the very, very low concentration  
 651 grains have corresponding low counts and therefore high uncertainty, and are therefore rejected. The rutile in this study has  
 652 significantly lower U concentrations than many other studies (Figure S12). There is a good reason to reject data with high

653 uncertainty, because they do not allow geologically significant dates to be calculated. In contrast, using a filter based on  
654 element abundance (i.e., the 4-5 ppm U threshold used in some publications) is dependent on abundance sensitivity (cps/ppm),  
655 which depends on the instrument (laser and ICP-MS type) and instrument settings. Isotopic and elemental concentrations are  
656 calculated based on the measured count rate (i.e., counts per second, CPS), which is inherently dependent on the individual  
657 mass spectrometer and laser ablation parameters (e.g., spot size, fluence). For instruments with lower sensitivity (lower CPS  
658 per ppm), the same calculated concentration (i.e., ~~the 4-5 ppm threshold used in some publications~~) yields lower CPS and  
659 therefore higher analytical uncertainties than for instruments with higher sensitivity. In this way, the U threshold filter based  
660 on a calculated concentration is instrument and parameter dependent and we therefore do not recommend this approach of  
661 screening rutile to exclude low U concentration analyses.

662 Most studies no longer impose a U threshold, yet, it is a regional concern in Türkiye where two of the four detrital  
663 rutile U-Pb datasets only analyze U-Pb on detrital rutile with uranium concentrations above 4-5 ppm (Okay et al., 2011;  
664 Şengün et al., 2020). The two studies that do not use a U filter analyze all detrital rutile grains (Shaanan et al., 2020; this  
665 study). In this dataset of this study, 87% of detrital rutile are below 4 ppm U (n=537/612). The majority of detrital rutile with  
666  $U > 4$  ppm are classified as pelitic and generally have higher Zr contents (higher temperature), whereas low-U rutile in this  
667 study generally correlates with lower Zr contents (lower temperature) and includes the majority of mafic-classified grains  
668 (Figure 9). Note that there are limitations to the Zr-in-rutile thermometer in mafic rocks if the equilibrium conditions are not  
669 met. 13 compares U concentration with concordance and U-Pb date. Concordance does not appear to be correlated with U  
670 concentration (13a). Comparing the date distribution for all grains with that of the groups of grains below and above 4 ppm  
671 U groups reveals that provenance results would be biased by excluding grains below 4 ppm U (13c). The above 4 ppm U  
672 group has age modes at 100 Ma, 165 Ma, 315 Ma, 458 Ma, and 600 Ma (13c pink) whereas the total date spectrum has peaks  
673 at 185 Ma, 300 Ma, 400 Ma, 450 Ma and 600 Ma (13c gray). The above 4 ppm U rutile group has higher amplitude  
674 Paleozoic peaks, a minor 100 Ma peak, and a younger, lower amplitude Mesozoic peak (165 Ma vs 185 Ma). In summary,  
675 the U threshold filter introduces bias into the provenance results because omitting low-U rutile biases results toward  
676 metapelitic sources, higher Zr-in-rutile temperatures, and shifts the prominent date modes and their amplitudes.





677  
 678 *Figure. Comparison of detrital rutile filtering based on U concentration or concordance. (A) Rutile U concentration versus*  
 679 *percent concordance (Stacey-Kramers distance). The U-threshold filter groups grains greater than and less than 4 ppm U. (B)*  
 680 *Rutile U-Pb results in Tera-Wasserburg space following the color scheme in panel A. (C) Rutile U concentration versus <sup>207</sup>Pb-*  
 681 *corrected U-Pb date. The relative KDEs display the date spectra from the different U concentration groups: all analyses,*  
 682 *above 4 ppm U, below 4 ppm U. The power law filter is applied to all plots in the figure.*  
 683

### 684 7.3 Source Protolith and Metamorphism

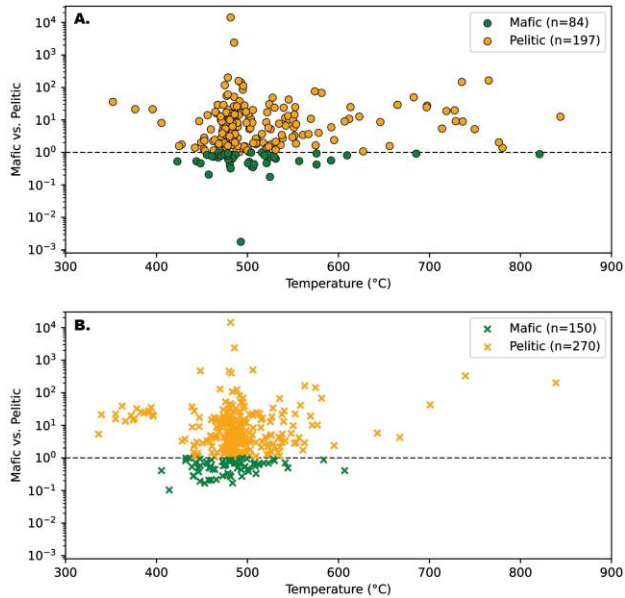
685 The Zr-in-rutile thermometer generally preserves the crystallization or recrystallization temperature. The Zr-in-rutile  
 686 thermometer can become uncoupled from the U-Pb age because Pb diffusion during medium- to high-temperature  
 687 metamorphic events or extended cooling periods will cause partial or complete resetting of the U-Pb system (Cherniak et al.,  
 688 2007; Luvizotto and Zack, 2009; Kooijman et al., 2012; Pereira and Storey, 2023). Because temperatures calculated for the

689 185 Ma population are cooler than for the older events and are not high enough to have reset the U-Pb dates, we interpret these  
690 temperatures as primary. Furthermore, partially reset dates would smear the data along concordia from the initial crystallization  
691 event age, not towards common Pb.

692 The Zr-in-rutile temperatures and protolith classification are discussed in [Section 8](#) ~~the following section~~ in the context  
693 of regional provenance. ~~The PCA results show that the first two principal components are explained by Cr, Nb and Ta, and W,  
694 Zr, and Hf. These elements are protolith (Cr, Nb, Ta) and temperature (Zr, Hf) dependent, therefore the protolith and Zr-in-  
695 rutile sections are already exploring the most salient aspects of the trace element dataset.~~

#### 696 7.4 Evaluating Bias in Discarded U-Pb Data

697 To evaluate the potential bias in U-Pb data reduction and processing, the detrital rutile grains with both U-Pb and  
698 trace element data are compared to those with only trace element data (U-Pb rejected and/or excluded by filter). Figure 14  
699 gives a sense for what data are missing from the U-Pb results as well as the effects of the uncertainty filter. ~~Note that not~~  
700 all detrital rutile grains have trace element data, so the subset of grains with U-Pb analyses and without trace element data  
701 cannot be considered. In the plots of protolith versus Zr-in-rutile temperature, grains included by the power law filter (Figure  
702 14a) are compared to those excluded by the power law filter or without U-Pb data (Figure 14b). Effectively this compares  
703 accepted U-Pb analyses to those rejected from unacceptable U-Pb signal patterns or high uncertainties. About 30% of mafic-  
704 classified grains and 35% of pelitic-classified grains are acceptable U-Pb analyses included by the power law filter (Figure  
705 14c). The analyses rejected by power law filtering (Figure 14c) have a similar temperature distribution, with the majority of  
706 temperatures from 450–550 °C. Most grains with these temperatures fall within the 185 Ma date mode (Figure 11), potentially  
707 suggesting that the detrital rutile grains with poor U-Pb precision would have ~185 Ma dates. Further, the rejected analyses  
708 group has fewer high temperature pelitic grains (> 600 °C) and a more abundant lower temperature pelitic population (< 400  
709 °C). These temperature windows do not seem diagnostic of specific date populations among pelitic grains, however, about  
710 30% of high temperature pelitic grains fall within the 500-650 Ma population (Figure 11). The similarity in temperature  
711 distributions of pelitic and mafic grains between the accepted and rejected U-Pb analyses suggests that there is not significant  
712 bias in the U-Pb results due to data rejection. Consequently, we suggest that the U-Pb and trace element data can be used  
713 together to interrogate potential bias in U-Pb data rejection and filtering.



714  
715  
716  
717  
718

Figure 14. (A) Protolith versus Zr-in-rutile temperature plot displays all detrital rutile analyses with trace element data included in the power law filter. (B) Plot B shows both the detrital rutile analyses without U-Pb data and those excluded by the power law filter in A. The y-axis values are the transformed distance from the mafic-pelitic discrimination line of Triebold et al. (2012) (Figure 9).

719

## 8 Anatolian Sedimentary Provenance

720

721

722

723

724

725

726

727

728

729

Sedimentary provenance is interpreted from all detrital rutile dates together, rather than by sample, due to the small number of analyses in each sample (see Figure S7 for individual sample results). The detrital rutile results are displayed along with detrital zircon dates from the same Upper Cretaceous to Eocene units in the Central Sakarya and Sarıcakaya Basins (Figure 15; data from Campbell, 2017; Ocakoğlu et al., 2018; Mueller et al., 2019, 2022; Okay and Kylander-Clark, 2022). The detrital zircon and rutile provenance results are discussed together from youngest to oldest date population. The rutile grains that (poorly) define the ca. 90 Ma population (Figure 15) include some of the highest Zr-in-rutile temperatures (Figure 11). The zircon record has abundant Late Cretaceous and Eocene populations (Figure 15) associated with magmatic flare-ups during Alpine orogeny-related subduction and syn-collisional magmatism, respectively (Harris et al., 1994; Kasapoğlu et al., 2016; Yıldız et al., 2015; Ocakoğlu et al., 2018; Mueller et al., 2022; Campbell et al., 2023). The lower plate Anatolide-Tauride terrane underwent HP/LT blueschist facies metamorphism that generally youngs from Late Cretaceous in the north to early

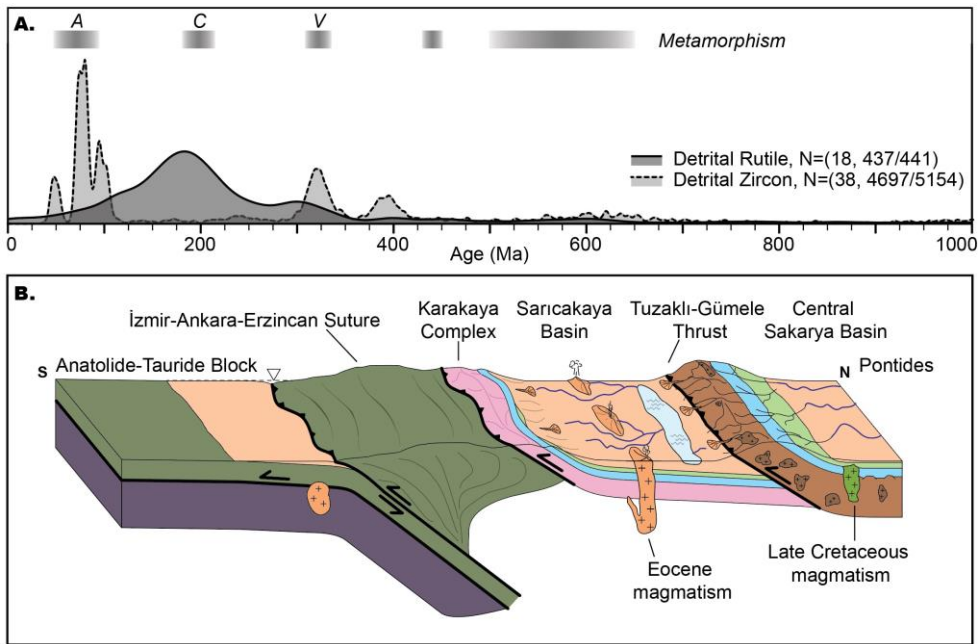
730 Eocene in the south (Sherlock et al., 1999; Okay and Kelley, 1994; Candan et al., 2005; Pourteau et al., 2016). However,  
731 the samples are from sedimentary basins on the Pontides upper plate (Figure 15) and the detrital zircon record indicates  
732 no sediment transport across the suture zone between from the Anatolide-Tauride terranes to the Pontides in the latest  
733 Cretaceous (Okay and Kylander-Clark, 2022). Thus, we interpret the 90 Ma rutile population as either igneous or metamorphic  
734 rutile derived from Late Cretaceous magmatism and associated contact metamorphism on the Pontides.

735 The 185 Ma peak includes the lowest Zr-in-rutile temperatures (~450–550 °C; Figure 11), mafic and pelitic sources  
736 (Figure 9), and predominantly low U rutile (13). The age, lithology, and temperature findings support a Karakaya Complex  
737 sediment source. The Permian–Triassic Karakaya Complex contains intra-oceanic basalts and forearc deposits that were  
738 metamorphosed to blueschist and epidote-amphibolite facies (340–550 ± 50 °C; Okay et al., 2002; Federici et al., 2010) during  
739 the Triassic Cimmerian event. The rutile U-Pb dates interpreted as Karakaya Complex (broad 185 Ma peak) are younger than  
740 existing Karakaya Complex phengite, glaucophane, and barrosite Ar-Ar cooling dates (~200–215 Ma; Okay et al., 2002;  
741 Federici et al., 2010; Şengör et al., 1984). The closure temperature windows for rutile U-Pb and phengite Ar-Ar overlap, with  
742 Pb in rutile extending to lower temperature than Ar in phengitic white mica (Itaya, 2020; M. Grove, pers. comm., 2024). The  
743 younger rutile dates likely indicate protracted cooling because extended time spent in the partial retention zone would cause  
744 variable Pb loss that could lead to a younger rutile U-Pb dates than any actual heating event and/or a spread in ages (broad  
745 peak). This 185 Ma population is not prominent in the detrital zircon spectra. Detrital zircons from Karakaya Complex units  
746 have age modes at ca. 235 Ma, 315 Ma, and 400 Ma and are interpreted as sediment input to the forearc from the Pontides  
747 Triassic magmatic arc, oceanic plateau, or spreading center (e.g., Okay et al., 2015), Variscan granitoids, and crystalline  
748 basement (Ustaömer et al., 2016).

749 The Carboniferous peaks in the zircon and rutile record correspond to a ~330–340 Ma pulse of high-T metamorphism  
750 and ~290–320 Ma magmatism in the Pontides during the Variscan orogeny (Topuz et al., 2007, 2020; Ustaömer et al., 2012,  
751 2013). Variscan-aged detrital rutiles were found in Jurassic sandstones in the Central Sakarya Basin and interpreted as derived  
752 from either primary Pontide basement or recycled sedimentary sources (Şengün et al., 2020). The Pontide basement units crop  
753 out along the Tuzaklı-Gümele Thrust fault that partitions the two sedimentary basins (Tuzaklı-Gümele Thrust; Figure  
754 15(b,b)). Therefore, the Variscan-aged detrital rutile could be derived from primary basement sources or recycled Jurassic  
755 sedimentary present in Upper Cretaceous to Eocene units, could be derived from primary basement sources or recycled Jurassic  
756 sedimentary units. The Pontides crystalline basement contains scarce Devonian (380–400 Ma) and Silurian (420–440 Ma)  
757 metaigneous rocks, which are exposed in the hanging wall of the Tuzaklı-Gümele Thrust (Topuz et al., 2020). The  
758 paucity/absence of this age population in the rutile record could be due to the scarcity of outcrops, small sample size, dilution  
759 during sediment recycling, or overprinting by the Carboniferous high temperature event. Late Ordovician–Early Silurian  
760 metamorphism associated with the accretion of the Istanbul–Moesia–Scythian Platform (Okay et al., 2006) is not prominent  
761 in the detrital rutile record, which could suggest the absence of major south-directed sediment transport across the Pontides  
762 (i.e., from the Istanbul Zone to Sakarya Zone across Intra-Pontide ocean/suture) during the Late Cretaceous to Eocene. Lastly,  
763 the 500–650 Ma Pan-African detrital rutile ages align with the detrital zircon age spectra. Gondwana-derived terranes are

764 characterized by Neoproterozoic–Cambrian plutonism and metamorphism from the Pan-African–Cadomian orogeny, which is  
 765 not well documented in Anatolia (Okay et al., 2006). Grains of this age could be sourced from the Pontides basement or  
 766 recycled from sedimentary units (Ustaömer et al., 2012; Mueller et al., 2019). However, if the grains of this age were first-  
 767 cycle from crystalline basement sources, we would expect them to have reset, younger U-Pb dates reflective of from-younger  
 768 metamorphic reheating events. However, by in this reasoning interpretation, the presence of 500–650 Ma dates indicates that are  
 769 preserved because these grains must have been unaffected by the any younger high-T events (i.e., Variscan, Cimmerian and  
 770 Alpine metamorphism). In order to have escaped metamorphic reheating, the grains had to have been already eroded from the  
 771 crystalline basement and deposited in sedimentary units. Therefore, we interpret the 500–650 Ma grains as polycyclic grains  
 772 derived from recycled sedimentary units. Together, the detrital zircon and rutile age spectra demonstrate that, from the Late  
 773 Cretaceous to Eocene, sediment was routed to the Central Sakarya and Sarıcakaya Basins from syn-depositional magmatic  
 774 centers, the Karakaya Complex within the suture zone, the Pontides crystalline basement, and recycled sedimentary units  
 775 (Figure 15).

776



777

778 *Figure 15. (A) Kernel density estimate of all detrital rutile dates (<sup>207</sup>Pb-corrected, power law uncertainty filtered) shown*  
779 *alongside a compilation of all published detrital zircon ages from Upper Cretaceous to Eocene strata in Central Sakarya and*  
780 *Sarıcakaya Basins. Gray bars depict periods of metamorphism in western Anatolia. (B) Schematic reconstruction of*  
781 *northwestern Anatolia in the Eocene during continental collision (after Mueller et al., 2019). The main sources of sediment*  
782 *to the basins were the Karakaya Complex exposed in the suture zone, Pontides crystalline basement exposed along the Tuzaklı-*  
783 *Gümele Thrust, Cretaceous-Eocene igneous units, and recycled sedimentary units. A: Alpine metamorphism, C: Cimmerian*  
784 *metamorphism, V: Variscan metamorphism.*

## 785 **9 Conclusions**

786 This work provides a systematic exploration of the data reduction and processing workflows for detrital rutile U-Pb  
787 geochronology using a new dataset from the Central Sakarya and Sarıcakaya Basins in Anatolia. Provenance interpretations  
788 are made from combining U-Pb dates and trace element geochemistry. The results have several implications for navigating  
789 workflows and interpretations in common Pb bearing detrital minerals:

790 (1) Natural datasets can be complex. While attempting a large-*n* provenance study, a significant number of analyses  
791 were discarded due to unacceptable U-Pb signal intensity and stability, namely low U, low Pb, and inclusions. This hurdle is  
792 evidently not unique to this dataset and should always be reported in detrital rutile U-Pb geochronology. Advances are needed  
793 to determine the best path forward, such as analyzing more grains for achieving large-*n* detrital rutile U-Pb datasets and more  
794 rigorous data reporting and standardizing metrics used for evaluating ‘acceptable’ U-Pb analyses. We recommend that the  
795 criteria for data rejection be explicitly discussed in all detrital rutile studies.

796 (2) We provide a method for evaluating the potential bias in U-Pb data rejection and filtering by comparing the detrital  
797 rutile grains with both U-Pb and trace element data to those with only trace element data. The ~~U-Pb~~ rejected and filtered out  
798 grains have a similar trace element distribution in terms of Zr-in-rutile temperature and mafic-pelitic classification to those  
799 with acceptable U-Pb analyses, suggesting there is not significant bias from U-Pb data rejection and filtering.

800 (3) The <sup>208</sup>Pb and <sup>207</sup>Pb correction methods produce similar age spectra and do not change the final provenance  
801 interpretations. Similarly, the uncertainty filters—based on U-Pb ratio uncertainty and corrected date uncertainty—produce  
802 similar date spectra. The power law uncertainty filter is preferred because it does not alter the date distribution and includes  
803 the most grains.

804 (4) There has not been an agreed upon metric to quantify discordance in common Pb minerals. We evaluate ~~various~~  
805 ~~the~~ ~~Stacey-Kramers and Aitchison~~ distance metrics (Text S3) and recommend the Stacey-Kramers distance as a suitable metric  
806 for quantifying discordance. However, because reliable interpretations can be made from analyses with significant proportions  
807 of common Pb, we ~~do not~~ ~~not~~ recommend applying a discordance filter to common Pb detrital minerals.

808 (5) In some labs and geographic locations, only rutile above a certain uranium concentration (i.e., 4-5 ppm U) are  
809 analyzed for U-Pb. We demonstrate that excluding low-U rutile biases provenance interpretations toward grains with pelitic  
810 ~~protolith~~ ~~classification~~, higher Zr-in-rutile temperatures, and higher concordance, and changes the overall date distribution,  
811 especially the amplitude of date peaks.

812 (6) A significant challenge in provenance work is pinpointing the signature of sediment recycling. Here we use paired  
813 U-Pb dates and Zr-in-rutile temperatures to identify polycyclic detrital rutile grains. The recycled grains preserve U-Pb dates  
814 that indicate that they escaped younger metamorphic reheating events of the crystalline basement by already being eroded and  
815 deposited in sedimentary units. In this way, detrital rutile petrochronology can address problems of sediment recycling.

816 (7) The data processing workflows used here are provided as code in Jupyter Notebooks that can be used by future  
817 studies. The code includes common Pb corrections, uncertainty filters, discordance calculations, ~~and principal component~~  
818 ~~analysis of trace element data, and other~~ trace element plots. The provided code is one path forward to achieving the required  
819 documentation and unification of data reduction approaches.

#### 820 **Data and code availability**

821 All of the data generated in this manuscript are publicly archived and available in an Open Science Framework data  
822 repository that can be accessed at <https://doi.org/10.17605/OSF.IO/A4YE5> (Mueller et al., 2023). The data repository also  
823 includes the supporting information text. Jupyter Notebooks containing the Python and R code used for data reduction and  
824 visualization are open and available at <https://zenodo.org/doi/10.5281/zenodo.10636727> (Mueller, 2024).

#### 825 **Author contributions**

826 MAM conceptualized the project; MAM and AL acquired funding; all authors were involved in the investigation;  
827 MAM and AM performed the formal data collection; all authors contributed to writing and revising the manuscript.

#### 828 **Competing interests**

829 The authors declare that they have no conflict of interest.

#### 830 **Disclaimer**

831 The software described here is provided under the Apache License, Version 2.0. It is provided "as is," without  
832 warranty of any kind, express or implied, including but not limited to the warranties of merchantability, fitness for a particular  
833 purpose, and noninfringement. In no event shall the authors or copyright holders be liable for any claim, damages, or other  
834 liability, whether in an action of contract, tort, or otherwise, arising from, out of, or in connection with the software or the use  
835 or other dealings in the software.

836 **Acknowledgements**

837 We thank Çelik Ocakoğlu, Jan Westerweel, Kate Huntington, Alison Duvall, Scott Braswell, Joel DesOrmeau, Sean  
838 Mulcahy, Scott Dakins, and Eric Steig for support in the field and lab. We thank Andrew Kylander-Clark, Francisco Apen,  
839 and Peter Downes for reference materials and Stuart Thomson, Margo Odlum, Eirini Poulaki, and Drew Levy for discussions  
840 on common Pb corrections. ~~We thank the jolite team for student access.~~ We thank Associate Editor Pieter Vermeesch and  
841 referees David Chew, Laura Bracciali, and Ines Pereira and an anonymous reviewer for thoughtful reviews that improved the  
842 manuscript. ~~We thank the jolite team for student access.~~

Formatted: Font: Not Italic

Formatted: Font: Not Italic

843 **Financial support**

844 This work was funded by the University of Washington Department of Earth and Space Sciences and NSF EAR-  
845 1543684 and EAR-2141115.

846 **References**

- 847 Açıkalın, S., Ocakoğlu, F., Yılmaz, İ. Ö., Vonhof, H., Hakyemez, A., and Smit, J.: Stable isotopes and geochemistry of a  
848 Campanian–Maastrichtian pelagic succession, Mudurnu–Göynük Basin, NW Turkey: Implications for palaeoceanography,  
849 palaeoclimate and sea-level fluctuations, *Palaeogeogr. Palaeoclimatol. Palaeoecol.*, 441, 453–466,  
850 <https://doi.org/10.1016/j.palaeo.2015.10.005>, 2016.
- 851 Aitchison, J.: The Statistical Analysis of Compositional Data, *J. R. Stat. Soc. Ser. B Methodol.*, 44, 139–177, 1982.
- 852 Aksay, A., Pehlivan, Ş., Gedik, I., Bilginer, E., Duru, M., Akbaş, B., and Altun, I.: Geologic map of Turkey (Zonguldak, Scale  
853 1:500,000), Maden Tetkik ve Arma Genel Müdürlüğü, Ankara, Turkey, 2002.
- 854 Andersen, T.: Correction of common lead in U–Pb analyses that do not report 204Pb, *Chem. Geol.*, 192, 59–79,  
855 [https://doi.org/10.1016/S0009-2541\(02\)00195-X](https://doi.org/10.1016/S0009-2541(02)00195-X), 2002.
- 856 Angiboust, S. and Harlov, D.: Ilmenite breakdown and rutile-titanite stability in metagranitoids: Natural observations and  
857 experimental results, *Am. Mineral.*, 102, 1696–1708, <https://doi.org/10.2138/am-2017-6064>, 2017.
- 858 Apen, F. E., Rudnick, R. L., Cottle, J. M., Kylander-Clark, A. R. C., Blondes, M. S., Piccoli, P. M., and Seward, G.: Four-  
859 dimensional thermal evolution of the East African Orogen: accessory phase petrochronology of crustal profiles through the  
860 Tanzanian Craton and Mozambique Belt, northeastern Tanzania, *Contrib. Mineral. Petrol.*, 175, 97,  
861 <https://doi.org/10.1007/s00410-020-01737-6>, 2020.
- 862 Blackburn, T. J., Bowring, S. A., Perron, J. T., Mahan, K. H., Dudas, F. O., and Barnhart, K. R.: An Exhumation History of  
863 Continents over Billion-Year Time Scales, *Science*, 335, 73–76, <https://doi.org/10.1126/science.1213496>, 2012.
- 864 Blum, M. and Pecha, M.: Mid-Cretaceous to Paleocene North American drainage reorganization from detrital zircons,  
865 *Geology*, 42, 607–610, <https://doi.org/10.1130/G35513.1>, 2014.



- 866 Bracciali, L.: Coupled Zircon-Rutile U-Pb Chronology: LA ICP-MS Dating, Geological Significance and Applications to  
867 Sediment Provenance in the Eastern Himalayan-Indo-Burman Region, *Geosciences*, 9, 467,  
868 <https://doi.org/10.3390/geosciences9110467>, 2019.
- 869 Bracciali, L., Parrish, R. R., Horstwood, M. S. A., Condon, D. J., and Najman, Y.: UPb LA-(MC)-ICP-MS dating of rutile:  
870 New reference materials and applications to sedimentary provenance, *Chem. Geol.*, 347, 82–101,  
871 <https://doi.org/10.1016/j.chemgeo.2013.03.013>, 2013.
- 872 Campbell, C. F.: Tectonic Evolution of the Izmir-Ankara Suture Zone in Northwest Turkey using Zircon U-Pb Geochronology  
873 and Zircon Lu-Hf Isotopic Tracers, M.S., University of Kansas, United States -- Kansas, 99 pp., 2017.
- 874 Campbell, C. F., Mueller, M. A., Taylor, M. H., Ocañoğlu, F., Möller, A., Métais, G., Coster, P. M. C., Beard, K. C., and Licht,  
875 A.: The Geodynamic Implications of Passive Margin Subduction in Northwest Turkey, *Geochem. Geophys. Geosystems*, 24,  
876 e2022GC010481, <https://doi.org/10.1029/2022GC010481>, 2023.
- 877 Candan, O., Çetinkaplan, M., Oberhänsli, R., Rimmelé, G., and Akal, C.: Alpine high-P/low-T metamorphism of the Afyon  
878 Zone and implications for the metamorphic evolution of Western Anatolia, Turkey, *Lithos*, 84, 102–124,  
879 <https://doi.org/10.1016/j.lithos.2005.02.005>, 2005.
- 880 Caracciolo, L., Ravidà, D. C. G., Chew, D., Janßen, M., Lünsdorf, N. K., Heins, W. A., Stephan, T., and Stollhofen, H.:  
881 Reconstructing environmental signals across the Permian-Triassic boundary in the SE Germanic Basin: A Quantitative  
882 Provenance Analysis (QPA) approach, *Glob. Planet. Change*, 206, 103631, <https://doi.org/10.1016/j.gloplacha.2021.103631>,  
883 2021.
- 884 Carrapa, B.: Resolving tectonic problems by dating detrital minerals, *Geology*, 38, 191–192,  
885 <https://doi.org/10.1130/focus022010.1>, 2010.
- 886 Cave, B. J., Stepanov, A. S., Craw, D., Large, R. R., Halpin, J. A., and Thompson, J.: RELEASE OF TRACE ELEMENTS  
887 THROUGH THE SUB-GREENSCHIST FACIES BREAKDOWN OF DETRITAL RUTILE TO METAMORPHIC  
888 TITANITE IN THE OTAGO SCHIST, NEW ZEALAND, *Can. Mineral.*, 53, 379–400,  
889 <https://doi.org/10.3749/canmin.1400097>, 2015.
- 890 Chermiak, D. J.: Pb diffusion in rutile, *Contrib. Mineral. Petrol.*, 139, 198–207, <https://doi.org/10.1007/PL00007671>, 2000.
- 891 Chermiak, D. J., Manchester, J., and Watson, E. B.: Zr and Hf diffusion in rutile, *Earth Planet. Sci. Lett.*, 261, 267–279,  
892 <https://doi.org/10.1016/j.epsl.2007.06.027>, 2007.
- 893 Chew, D., O’Sullivan, G., Caracciolo, L., Mark, C., and Tyrrell, S.: Sourcing the sand: Accessory mineral fertility, analytical  
894 and other biases in detrital U-Pb provenance analysis, *Earth-Sci. Rev.*, 202, 103093,  
895 <https://doi.org/10.1016/j.earscirev.2020.103093>, 2020.
- 896 Chew, D. M., Sylvester, P. J., and Tubrett, M. N.: U–Pb and Th–Pb dating of apatite by LA-ICPMS, *Chem. Geol.*, 280, 200–  
897 216, <https://doi.org/10.1016/j.chemgeo.2010.11.010>, 2011.
- 898 Chew, D. M., Petrus, J. A., and Kamber, B. S.: U-Pb LA-ICPMS dating using accessory mineral standards with variable  
899 common Pb, *Chem. Geol.*, 363, 185–199, <https://doi.org/10.1016/j.chemgeo.2013.11.006>, 2014.
- 900 Clark, D. J., Hensen, B. J., and Kinny, P. D.: Geochronological constraints for a two-stage history of the Albany–Fraser  
901 Orogen, Western Australia, *Precambrian Res.*, 102, 155–183, [https://doi.org/10.1016/S0301-9268\(00\)00063-2](https://doi.org/10.1016/S0301-9268(00)00063-2), 2000.

- 902 Clift, P. D., Hodges, K. V., Heslop, D., Hannigan, R., Van Long, H., and Calves, G.: Correlation of Himalayan exhumation  
903 rates and Asian monsoon intensity, *Nat. Geosci.*, 1, 875–880, <https://doi.org/10.1038/ngeo351>, 2008.
- 904 Clift, P. D., Mark, C., Alizai, A., Khan, H., and Jan, M. Q.: Detrital U–Pb rutile and zircon data show Indus River sediment  
905 dominantly eroded from East Karakoram, not Nanga Parbat, *Earth Planet. Sci. Lett.*, 600, 117873,  
906 <https://doi.org/10.1016/j.epsl.2022.117873>, 2022.
- 907 Compston, W., Williams, I. S., and Meyer, C.: U–Pb geochronology of zircons from lunar breccia 73217 using a sensitive high  
908 mass-resolution ion microprobe, *J. Geophys. Res. Solid Earth*, 89, B525–B534, <https://doi.org/10.1029/JB089iS02p0B525>,  
909 1984.
- 910 Crameri, F., Shephard, G. E., and Heron, P. J.: The misuse of colour in science communication, *Nat. Commun.*, 11, 5444,  
911 <https://doi.org/10.1038/s41467-020-19160-7>, 2020.
- 912 Davis, W. J., Canil, D., MacKenzie, J. M., and Carbno, G. B.: Petrology and U–Pb geochronology of lower crustal xenoliths  
913 and the development of a craton, Slave Province, Canada, *Lithos*, 71, 541–573, [https://doi.org/10.1016/S0024-4937\(03\)00130-](https://doi.org/10.1016/S0024-4937(03)00130-0)  
914 0, 2003.
- 915 Dickinson, W. R. and Suczek, C. A.: Plate Tectonics and Sandstone Compositions, *AAPG Bull.*, 63, 2164–2182, 1979.
- 916 Dodson, M. H.: Closure Temperature in Cooling Geochronological and Petrological Systems, *Contrib. Mineral. Petrol.*, 40,  
917 259–274, 1973.
- 918 Ershova, V., Prokopyev, A., and Stockli, D.: Provenance of Detrital Rutiles from the Triassic–Jurassic Sandstones in Franz  
919 Josef Land (Barents Sea Region, Russian High Arctic): U–Pb Ages and Trace Element Geochemistry, *Geosciences*, 14, 41,  
920 <https://doi.org/10.3390/geosciences14020041>, 2024.
- 921 Ersoy, E. Y., Akal, C., Genç, Ş. C., Candan, O., Palmer, M. R., Prelević, D., Uysal, İ., and Mertz-Kraus, R.: U–Pb zircon  
922 geochronology of the Paleogene – Neogene volcanism in the NW Anatolia: Its implications for the Late Mesozoic–Cenozoic  
923 geodynamic evolution of the Aegean, *Tectonophysics*, 717, 284–301, <https://doi.org/10.1016/j.tecto.2017.08.016>, 2017.
- 924 Ersoy, E. Y., Akal, C., Palmer, M. R., and Mertz-Kraus, R.: U–Pb dating of arc to post-collisional magmatic events in  
925 northwestern Anatolia: The Eocene Granitoids in NW Anatolia revisited, *J. Asian Earth Sci.* X, 9, 100148,  
926 <https://doi.org/10.1016/j.jaesx.2023.100148>, 2023.
- 927 Ewing, T. A.: Hf isotope analysis and U–Pb geochronology of rutile : technique development and application to a lower crustal  
928 section (Ivrea-Verbanò Zone, Italy), <https://doi.org/10.25911/5d74e68841e8d>, 2011.
- 929 Ewing, T. A., Rubatto, D., Beltrando, M., and Hermann, J.: Constraints on the thermal evolution of the Adriatic margin during  
930 Jurassic continental break-up: U–Pb dating of rutile from the Ivrea–Verbanò Zone, Italy, *Contrib. Mineral. Petrol.*, 169, 44,  
931 <https://doi.org/10.1007/s00410-015-1135-6>, 2015.
- 932 Faure, G.: *Principles of Isotope Geology*, 2nd Edition., Wiley & Sons, Inc., 608 pp., 1986.
- 933 Federici, I., CAVAZZA, W., OKAY, A. I., BEYSSAC, O., ZATTIN, M., CORRADO, S., and DELLISANTI, F.: Thermal  
934 Evolution of the Permo–Triassic Karakaya Subduction-accretion Complex between the Biga Peninsula and the Tokat Massif  
935 (Anatolia), *Turk. J. Earth Sci.*, 19, 409–429, <https://doi.org/10.3906/yer-0910-39>, 2010.
- 936 Ferry, J. M. and Watson, E. B.: New thermodynamic models and revised calibrations for the Ti-in-zircon and Zr-in-rutile  
937 thermometers, *Contrib. Mineral. Petrol.*, 154, 429–437, <https://doi.org/10.1007/s00410-007-0201-0>, 2007.

- 938 Flowers, R. M., Bowring, S. A., Tulloch, A. J., and Klepeis, K. A.: Tempo of burial and exhumation within the deep roots of  
939 a magmatic arc, Fiordland, New Zealand, *Geology*, 33, 17–20, <https://doi.org/10.1130/G21010.1>, 2005.
- 940 Foley, S. F., Barth, M. G., and Jenner, G. A.: Rutile/melt partition coefficients for trace elements and an assessment of the  
941 influence of rutile on the trace element characteristics of subduction zone magmas, *Geochim. Cosmochim. Acta*, 64, 933–938,  
942 [https://doi.org/10.1016/S0016-7037\(99\)00355-5](https://doi.org/10.1016/S0016-7037(99)00355-5), 2000.
- 943 Garzanti, E. and Andò, S.: Heavy Mineral Concentration in Modern Sands: Implications for Provenance Interpretation, in:  
944 *Developments in Sedimentology*, vol. 58, edited by: Mange, M. A. and Wright, D. T., Elsevier, 517–545,  
945 [https://doi.org/10.1016/S0070-4571\(07\)58020-9](https://doi.org/10.1016/S0070-4571(07)58020-9), 2007.
- 946 Garzanti, E., Doglioni, C., Vezzoli, G., and Ando, S.: Orogenic belts and orogenic sediment provenance, *J. Geol.*, 115, 315–  
947 334, 2007.
- 948 Gaschnig, R. M.: Benefits of a Multiproxy Approach to Detrital Mineral Provenance Analysis: An Example from the  
949 Merrimack River, New England, USA, *Geochem. Geophys. Geosystems*, 20, 1557–1573,  
950 <https://doi.org/10.1029/2018GC008005>, 2019.
- 951 Gazzi, P.: On the Heavy Mineral Zones in the Geosyncline Series. Recent Studies in the Northern Apennines, Italy, *J.*  
952 *Sediment. Petrol.*, 35, 109–115, <https://doi.org/10.1306/74D71203-2B21-11D7-8648000102C1865D>, 1965.
- 953 Gehrels, G.: Detrital Zircon U-Pb Geochronology: Current Methods and New Opportunities, in: *Tectonics of Sedimentary*  
954 *Basins*, John Wiley & Sons, Ltd, 45–62, <https://doi.org/10.1002/9781444347166.ch2>, 2011.
- 955 Gehrels, G.: Detrital Zircon U-Pb Geochronology Applied to Tectonics, *Annu. Rev. Earth Planet. Sci.*, 42, 127–149,  
956 <https://doi.org/10.1146/annurev-earth-050212-124012>, 2014.
- 957 Gehrels, G. E., Valencia, V. A., and Ruiz, J.: Enhanced precision, accuracy, efficiency, and spatial resolution of U-Pb ages by  
958 laser ablation–multicollector–inductively coupled plasma–mass spectrometry, *Geochem. Geophys. Geosystems*, 9, Q03017,  
959 <https://doi.org/10.1029/2007GC001805>, 2008.
- 960 Göncüoğlu, M. C., Turhan, N., Şentürk, K., Özcan, A., Uysal, Ş., and Yaliniz, M. K.: A Geotraverse Across Northwestern  
961 Turkey: Tectonic Units of the Central Sakarya Region and their Tectonic Evolution, *Geol. Soc. Lond. Spec. Publ.*, 173, 139–  
962 161, <https://doi.org/10.1144/GSL.SP.2000.173.01.06>, 2000.
- 963 Govin, G., Najman, Y., Copley, A., Millar, I., van der Beek, P., Huyghe, P., Grujic, D., and Davenport, J.: Timing and  
964 mechanism of the rise of the Shillong Plateau in the Himalayan foreland, *Geology*, 46, 279–282,  
965 <https://doi.org/10.1130/G39864.1>, 2018.
- 966 Guo, R., Hu, X., Garzanti, E., Lai, W., Yan, B., and Mark, C.: How faithfully do the geochronological and geochemical  
967 signatures of detrital zircon, titanite, rutile and monazite record magmatic and metamorphic events? A case study from the  
968 Himalaya and Tibet, *Earth-Sci. Rev.*, 201, 103082, <https://doi.org/10.1016/j.earscirev.2020.103082>, 2020.
- 969 Harris, N. B. W., Kelley, S., and Okay, A. I.: Post-collisional magmatism and tectonics in northwest Anatolia, *Contrib. Mineral.*  
970 *Petrol.*, 117, 241–252, 1994.
- 971 Hart, E., Storey, C., Bruand, E., Schertl, H.-P., and Alexander, B. D.: Mineral inclusions in rutile: A novel recorder of HP-  
972 UHP metamorphism, *Earth Planet. Sci. Lett.*, 446, 137–148, <https://doi.org/10.1016/j.epsl.2016.04.035>, 2016.

- 973 Hart, E., Storey, C., Harley, S. L., and Fowler, M.: A window into the lower crust: Trace element systematics and the  
974 occurrence of inclusions/intergrowths in granulite-facies rutile, *Gondwana Res.*, 59, 76–86,  
975 <https://doi.org/10.1016/j.gr.2018.02.021>, 2018.
- 976 Hietpas, J., Samson, S., Moecher, D., and Schmitt, A. K.: Recovering tectonic events from the sedimentary record: Detrital  
977 monazite plays in high fidelity, *Geology*, 38, 167–170, <https://doi.org/10.1130/G30265.1>, 2010.
- 978 Hietpas, J., Samson, S., Moecher, D., and Chakraborty, S.: Enhancing tectonic and provenance information from detrital zircon  
979 studies: assessing terrane-scale sampling and grain-scale characterization, *J. Geol. Soc.*, 168, 309–318,  
980 <https://doi.org/10.1144/0016-76492009-163>, 2011.
- 981 Hubert, J. F.: Analysis of heavy-mineral assemblages, in: *Procedures in sedimentary petrology*, edited by: Carver, R. E., New  
982 York: Wiley-Interscience, 453–478, 1971.
- 983 Itaya, T.: K–Ar phengite geochronology of HP–UHP metamorphic rocks –An in–depth review–, *J. Mineral. Petrol. Sci.*, 115,  
984 44–58, <https://doi.org/10.2465/jmps.190123>, 2020.
- 985 Jochum, K. P., Wilson, S. A., Abouchami, W., Amini, M., Chmeleff, J., Eisenhauer, A., Hegner, E., Iaccheri, L. M., Kieffer,  
986 B., Krause, J., McDonough, W. F., Mertz-Kraus, R., Raczek, I., Rudnick, R. L., Scholz, D., Steinhofel, G., Stoll, B., Stracke,  
987 A., Tonarini, S., Weis, D., Weis, U., and Woodhead, J. D.: GSD-1G and MPI-DING Reference Glasses for In Situ and Bulk  
988 Isotopic Determination, *Geostand. Geoanalytical Res.*, 35, 193–226, <https://doi.org/10.1111/j.1751-908X.2010.00114.x>, 2011.
- 989 Kasapoğlu, B., Ersoy, Y. E., Uysal, İ., Palmer, M. R., Zack, T., Koralay, E. O., and Karlsson, A.: The petrology of Paleogene  
990 volcanism in the Central Sakarya, Nallihan Region: Implications for the initiation and evolution of post-collisional, slab break-  
991 off-related magmatic activity, *Lithos*, 246–247, 81–98, <https://doi.org/10.1016/j.lithos.2015.12.024>, 2016.
- 992 Kellett, D. A., Weller, O. M., Zagorevski, A., and Regis, D.: A petrochronological approach for the detrital record: Tracking  
993 mm-sized eclogite clasts in the northern Canadian Cordillera, *Earth Planet. Sci. Lett.*, 494, 23–31,  
994 <https://doi.org/10.1016/j.epsl.2018.04.036>, 2018.
- 995 Keskin, M. and Tüysüz, O.: Stratigraphy, petrogenesis and geodynamic setting of Late Cretaceous volcanism on the SW  
996 margin of the Black Sea, Turkey, *Geol. Soc. Lond. Spec. Publ.*, 464, 95–130, <https://doi.org/10.1144/SP464.5>, 2018.
- 997 Klemme, S., Blundy, J. D., and Wood, B. J.: Experimental constraints on major and trace element partitioning during partial  
998 melting of eclogite, *Geochim. Cosmochim. Acta*, 66, 3109–3123, [https://doi.org/10.1016/S0016-7037\(02\)00859-1](https://doi.org/10.1016/S0016-7037(02)00859-1), 2002.
- 999 Kohn, M. J.: A refined zirconium-in-rutile thermometer, *Am. Mineral.*, 105, 963–971, <https://doi.org/10.2138/am-2020-7091>,  
1000 2020.
- 1001 Kohn, M. J. and Kelly, N. M.: Petrology and Geochronology of Metamorphic Zircon, in: *Geophysical Monograph Series*,  
1002 edited by: Moser, D. E., Corfu, F., Darling, J. R., Reddy, S. M., and Tait, K., John Wiley & Sons, Inc., Hoboken, NJ, USA,  
1003 35–61, <https://doi.org/10.1002/9781119227250.ch2>, 2017.
- 1004 Kooijman, E., Mezger, K., and Berndt, J.: Constraints on the U–Pb systematics of metamorphic rutile from in situ LA-ICP-  
1005 MS analysis, *Earth Planet. Sci. Lett.*, 293, 321–330, <https://doi.org/10.1016/j.epsl.2010.02.047>, 2010.
- 1006 Kooijman, E., Smit, M. A., Mezger, K., and Berndt, J.: Trace element systematics in granulite facies rutile: implications for  
1007 Zr geothermometry and provenance studies, *J. Metamorph. Geol.*, 30, 397–412, <https://doi.org/10.1111/j.1525-1314.2012.00972.x>, 2012.

- 1009 Kylander-Clark, A. R. C.: Slow subduction and exhumation of a thick ultrahigh -pressure terrane: Western Gneiss Region,  
1010 Norway, Ph.D., University of California, Santa Barbara, United States -- California, 121 pp., 2008.
- 1011 Kylander-Clark, A. R. C., Hacker, B. R., and Mattinson, J. M.: Slow exhumation of UHP terranes: Titanite and rutile ages of  
1012 the Western Gneiss Region, Norway, *Earth Planet. Sci. Lett.*, 272, 531–540, <https://doi.org/10.1016/j.epsl.2008.05.019>, 2008.
- 1013 Lippert, P. G.: Detrital U-Pb geochronology provenance analyses: case studies in the Greater Green River Basin, Wyoming,  
1014 and the Book Cliffs, Utah, Thesis, University of Kansas, 2014.
- 1015 Ludwig, K. R.: On the Treatment of Concordant Uranium-Lead Ages, *Geochim. Cosmochim. Acta*, 62, 665–676,  
1016 [https://doi.org/10.1016/S0016-7037\(98\)00059-3](https://doi.org/10.1016/S0016-7037(98)00059-3), 1998.
- 1017 Luvizotto, G. L. and Zack, T.: Nb and Zr behavior in rutile during high-grade metamorphism and retrogression: An example  
1018 from the Ivrea–Verbano Zone, *Chem. Geol.*, 261, 303–317, <https://doi.org/10.1016/j.chemgeo.2008.07.023>, 2009.
- 1019 Luvizotto, G. L., Zack, T., Meyer, H. P., Ludwig, T., Triebold, S., Kronz, A., Münker, C., Stockli, D. F., Prowatke, S., Klemme,  
1020 S., Jacob, D. E., and von Eynatten, H.: Rutile crystals as potential trace element and isotope mineral standards for  
1021 microanalysis, *Chem. Geol.*, 261, 346–369, <https://doi.org/10.1016/j.chemgeo.2008.04.012>, 2009.
- 1022 Malusà, M. G., Carter, A., Limoncelli, M., Villa, I. M., and Garzanti, E.: Bias in detrital zircon geochronology and  
1023 thermochronometry, *Chem. Geol.*, 359, 90–107, <https://doi.org/10.1016/j.chemgeo.2013.09.016>, 2013.
- 1024 Mark, C., Cogné, N., and Chew, D.: Tracking exhumation and drainage divide migration of the Western Alps: A test of the  
1025 apatite U-Pb thermochronometer as a detrital provenance tool, *GSA Bull.*, 128, 1439–1460, <https://doi.org/10.1130/B31351.1>,  
1026 2016.
- 1027 McLean, N. M., Bowring, J. F., and Bowring, S. A.: An algorithm for U-Pb isotope dilution data reduction and uncertainty  
1028 propagation, *Geochem. Geophys. Geosystems*, 12, <https://doi.org/10.1029/2010GC003478>, 2011.
- 1029 Meinhold, G.: Rutile and its applications in earth sciences, *Earth-Sci. Rev.*, 102, 1–28,  
1030 <https://doi.org/10.1016/j.earscirev.2010.06.001>, 2010.
- 1031 Meinhold, G., Anders, B., Kostopoulos, D., and Reischmann, T.: Rutile chemistry and thermometry as provenance indicator:  
1032 An example from Chios Island, Greece, *Sediment. Geol.*, 203, 98–111, <https://doi.org/10.1016/j.sedgeo.2007.11.004>, 2008.
- 1033 Meinhold, G., MORTON, A. C., FANNING, C. M., and WHITHAM, A. G.: U–Pb SHRIMP ages of detrital granulite-facies  
1034 rutiles: further constraints on provenance of Jurassic sandstones on the Norwegian margin, *Geol. Mag.*, 148, 473–480,  
1035 <https://doi.org/10.1017/S0016756810000877>, 2010.
- 1036 Mezger, K., Hanson, G. N., and Bohlen, S. R.: High-precision UPb ages of metamorphic rutile: application to the cooling  
1037 history of high-grade terranes, *Earth Planet. Sci. Lett.*, 96, 106–118, [https://doi.org/10.1016/0012-821X\(89\)90126-X](https://doi.org/10.1016/0012-821X(89)90126-X), 1989.
- 1038 Moecher, D., Hietpas, J., Samson, S., and Chakraborty, S.: Insights into southern Appalachian tectonics from ages of detrital  
1039 monazite and zircon in modern alluvium, *Geosphere*, 7, 494–512, <https://doi.org/10.1130/GES00615.1>, 2011.
- 1040 Möller, A., Mezger, K., and Schenk, V.: U–Pb dating of metamorphic minerals: Pan-African metamorphism and prolonged  
1041 slow cooling of high pressure granulites in Tanzania, East Africa, *Precambrian Res.*, 104, 123–146,  
1042 [https://doi.org/10.1016/S0301-9268\(00\)00086-3](https://doi.org/10.1016/S0301-9268(00)00086-3), 2000.

- 1043 Morton, A. and Yaxley, G.: Detrital apatite geochemistry and its application in provenance studies, *Geol. Soc. Am. Spec. Pap.*,  
1044 420, 319–344, [https://doi.org/10.1130/2006.2420\(19\)](https://doi.org/10.1130/2006.2420(19)), 2007.
- 1045 Morton, A. C.: Heavy minerals in provenance studies, in: *Provenance of Arenites*, edited by: Zuffa, G. G., Reidel, Dordrecht,  
1046 249–277, 1985.
- 1047 Mueller, M., Licht, A., Möller, A., Condit, C., Fosdick, J. C., Oçakoğlu, F., and Campbell, C.: Supplemental data for:  
1048 Navigating the complexity of detrital rutile provenance: Methodological insights from the Neotethys Orogen in Anatolia,  
1049 <https://doi.org/10.17605/OSF.IO/A4YE5>, 2023.
- 1050 Mueller, M. A.: mmueller13/Detrital-UPb-and-TE: v0.2, , <https://doi.org/10.5281/zenodo.10636728>, 2024.
- 1051 Mueller, M. A., Licht, A., Campbell, C., Oçakoğlu, F., Taylor, M. H., Burch, L., Ugrai, T., Kaya, M., Kurtoglu, B., Coster, P.  
1052 M. C., Métais, G., and Beard, K. C.: Collision Chronology Along the İzmir-Ankara-Erzincan Suture Zone: Insights From the  
1053 Sarıcakaya Basin, Western Anatolia, *Tectonics*, 38, 3652–3674, <https://doi.org/10.1029/2019TC005683>, 2019.
- 1054 Mueller, M. A., Licht, A., Campbell, C., Oçakoğlu, F., Akşit, G. G., Métais, G., Coster, P. M. C., Beard, K. C., and Taylor,  
1055 M. H.: Sedimentary Provenance From the Evolving Forearc-to-Foreland Central Sakarya Basin, Western Anatolia Reveals  
1056 Multi-Phase Intercontinental Collision, *Geochem. Geophys. Geosystems*, 23, e2021GC010232,  
1057 <https://doi.org/10.1029/2021GC010232>, 2022.
- 1058 Nemchin, A. A. and Cawood, P. A.: Discordance of the U–Pb system in detrital zircons: Implication for provenance studies  
1059 of sedimentary rocks, *Sediment. Geol.*, 182, 143–162, <https://doi.org/10.1016/j.sedgeo.2005.07.011>, 2005.
- 1060 Oçakoğlu, F., Hakyemez, A., Açıkalın, S., Özkan Altıner, S., Büyükmeriç, Y., Licht, A., Demircan, H., Şafak, Ü., Yıldız, A.,  
1061 Yılmaz, İ. Ö., Wagreich, M., and Campbell, C.: Chronology of subduction and collision along the İzmir-Ankara suture in  
1062 Western Anatolia: records from the Central Sakarya Basin, *Int. Geol. Rev.*, 1–26,  
1063 <https://doi.org/10.1080/00206814.2018.1507009>, 2018.
- 1064 Odlum, M. L., Stockli, D. F., Capaldi, T. N., Thomson, K. D., Clark, J., Puigdefàbregas, C., and Fildani, A.: Tectonic and  
1065 sediment provenance evolution of the South Eastern Pyrenean foreland basins during rift margin inversion and orogenic uplift,  
1066 *Tectonophysics*, 765, 226–248, <https://doi.org/10.1016/j.tecto.2019.05.008>, 2019.
- 1067 Okay, A., Satir, M., and Siebel, W.: Pre-Alpide Palaeozoic and Mesozoic Orogenic Events in the Eastern Mediterranean  
1068 Region, *Geol. Soc. Lond. Mem.*, 32, 389–405, <https://doi.org/10.1144/GSL.MEM.2006.032.01.23>, 2006.
- 1069 Okay, A. I. and Gönçüoğlu, M. C.: The Karakaya Complex: A Review of Data and Concepts, *Turk. J. Earth Sci.*, 13, 77–95,  
1070 2004.
- 1071 Okay, A. I. and Kelley, S. P.: Tectonic setting, petrology and geochronology of jadeite + glaucophane and chloritoid +  
1072 glaucophane schists from north-west Turkey, *J. Metamorph. Geol.*, 12, 455–466, <https://doi.org/10.1111/j.1525-1314.1994.tb00035.x>, 1994.
- 1074 Okay, A. I. and Kylander-Clark, A. R. C.: No sediment transport across the Tethys ocean during the latest Cretaceous: detrital  
1075 zircon record from the Pontides and the Anatolide–Tauride Block, *Int. J. Earth Sci.*, <https://doi.org/10.1007/s00531-022-02275-1>, 2022.
- 1077 Okay, A. I., Monod, O., and Monié, P.: Triassic blueschists and eclogites from northwest Turkey: vestiges of the Paleo-Tethyan  
1078 subduction, *Lithos*, 64, 155–178, [https://doi.org/10.1016/S0024-4937\(02\)00200-1](https://doi.org/10.1016/S0024-4937(02)00200-1), 2002.

- 1079 Okay, A. I., Altiner, D., and Kiliç, A. M.: Triassic limestone, turbidites and serpentinite—the Cimmeride orogeny in the Central  
1080 Pontides, *Geol. Mag.*, 152, 460–479, <https://doi.org/10.1017/S0016756814000429>, 2015.
- 1081 Okay, A. I., Sunal, G., Sherlock, S., Kylander-Clark, A. R. C., and Özcan, E.: İzmir-Ankara Suture as a Triassic to Cretaceous  
1082 Plate Boundary—Data From Central Anatolia, *Tectonics*, 39, e2019TC005849, <https://doi.org/10.1029/2019TC005849>, 2020.
- 1083 Okay, N., Zack, T., Okay, A. I., and Barth, M.: Sinistral transport along the Trans-European Suture Zone: detrital zircon–rutile  
1084 geochronology and sandstone petrography from the Carboniferous flysch of the Pontides, *Geol. Mag.*, 148, 380–403,  
1085 <https://doi.org/10.1017/S0016756810000804>, 2011.
- 1086 O’Sullivan, G., Chew, D., Kenny, G., Henrichs, I., and Mulligan, D.: The trace element composition of apatite and its  
1087 application to detrital provenance studies, *Earth-Sci. Rev.*, 201, 103044, <https://doi.org/10.1016/j.earscirev.2019.103044>,  
1088 2020.
- 1089 O’Sullivan, G. J., Chew, D. M., and Samson, S. D.: Detecting magma-poor orogens in the detrital record, *Geology*, 44, 871–  
1090 874, <https://doi.org/10.1130/G38245.1>, 2016.
- 1091 Paterson, S. R. and Ducea, M. N.: Arc Magmatic Tempos: Gathering the Evidence, *Elements*, 11, 91–98,  
1092 <https://doi.org/10.2113/gselements.11.2.91>, 2015.
- 1093 Paton, C., Hellstrom, J., Paul, B., Woodhead, J., and Hergt, J.: Iolite: Freeware for the visualisation and processing of mass  
1094 spectrometric data, *J. Anal. At. Spectrom.*, 26, 2508, <https://doi.org/10.1039/c1ja10172b>, 2011.
- 1095 Pawlowsky-Glahn, V., Egozcue, J. J., and Tolosana-Delgado, R.: *Modeling and Analysis of Compositional Data*, John Wiley  
1096 & Sons, Incorporated, Newark, UNITED STATES, 2015.
- 1097 Pereira, I. and Storey, C. D.: Detrital rutile: Records of the deep crust, ores and fluids, *Lithos*, 107010,  
1098 <https://doi.org/10.1016/j.lithos.2022.107010>, 2023.
- 1099 Pereira, I., Storey, C. D., Strachan, R. A., Bento dos Santos, T., and Darling, J. R.: Detrital rutile ages can deduce the tectonic  
1100 setting of sedimentary basins, *Earth Planet. Sci. Lett.*, 537, 116193, <https://doi.org/10.1016/j.epsl.2020.116193>, 2020.
- 1101 Pereira, I., Storey, C. D., Darling, J. R., Moreira, H., Strachan, R. A., and Cawood, P. A.: Detrital rutile tracks the first  
1102 appearance of subduction zone low T/P paired metamorphism in the Palaeoproterozoic, *Earth Planet. Sci. Lett.*, 570, 117069,  
1103 <https://doi.org/10.1016/j.epsl.2021.117069>, 2021.
- 1104 Pickett, E. A. and Robertson, A. H. F.: Formation of the Late Palaeozoic–Early Mesozoic Karakaya Complex and related  
1105 ophiolites in NW Turkey by Palaeotethyan subduction–accretion, *J. Geol. Soc.*, 153, 995–1009,  
1106 <https://doi.org/10.1144/gsjgs.153.6.0995>, 1996.
- 1107 Plavsa, D., Reddy, S. M., Agangi, A., Clark, C., Kylander-Clark, A., and Tiddy, C. J.: Microstructural, trace element and  
1108 geochronological characterization of TiO<sub>2</sub> polymorphs and implications for mineral exploration, *Chem. Geol.*, 476, 130–149,  
1109 <https://doi.org/10.1016/j.chemgeo.2017.11.011>, 2018.
- 1110 Poulaki, E. M., Stockli, D. F., and Shuck, B. D.: Pre-Subduction Architecture Controls Coherent Underplating During  
1111 Subduction and Exhumation (Nevado-Filábride Complex, Southern Spain), *Geochem. Geophys. Geosystems*, 24,  
1112 e2022GC010802, <https://doi.org/10.1029/2022GC010802>, 2023.
- 1113 Pourteau, A., Oberhänsli, R., Candan, O., Barrier, E., and Vrielynck, B.: Neotethyan closure history of western Anatolia: a  
1114 geodynamic discussion, *Int. J. Earth Sci.*, 105, 203–224, <https://doi.org/10.1007/s00531-015-1226-7>, 2016.

- 1115 Rösel, D., Boger, S. D., Möller, A., Gaitzsch, B., Barth, M., Oalmann, J., and Zack, T.: Indo-Antarctic derived detritus on the  
 1116 northern margin of Gondwana: evidence for continental-scale sediment transport, *Terra Nova*, 26, 64–71,  
 1117 <https://doi.org/10.1111/ter.12070>, 2014.
- 1118 Rösel, D., Zack, T., and Möller, A.: Interpretation and significance of combined trace element and U–Pb isotopic data of  
 1119 detrital rutile: a case study from late Ordovician sedimentary rocks of Saxo-Thuringia, Germany, *Int. J. Earth Sci.*, 108, 1–25,  
 1120 <https://doi.org/10.1007/s00531-018-1643-5>, 2019.
- 1121 Rudnick, R., Barth, M., Horn, I., and McDonough, W. F.: Rutile-Bearing Refractory Eclogites: Missing Link Between  
 1122 Continents and Depleted Mantle, *Science*, 287, 278–281, <https://doi.org/10.1126/science.287.5451.278>, 2000.
- 1123 Schärer, U., Krogh, T. E., and Gower, C. F.: Age and evolution of the Grenville Province in eastern Labrador from U-Pb  
 1124 systematics in accessory minerals, *Contrib. Mineral. Petrol.*, 94, 438–451, <https://doi.org/10.1007/BF00376337>, 1986.
- 1125 Schmitz, M. D. and Bowring, S. A.: Constraints on the thermal evolution of continental lithosphere from U-Pb accessory  
 1126 mineral thermochronometry of lower crustal xenoliths, southern Africa, *Contrib. Mineral. Petrol.*, 144, 592–618,  
 1127 <https://doi.org/10.1007/s00410-002-0419-9>, 2003.
- 1128 Schoene, B.: U–Th–Pb Geochronology, in: *Treatise on Geochemistry*, Elsevier, 341–378, <https://doi.org/10.1016/B978-0-08-095975-7.00310-7>, 2014.
- 1130 Şengör, A. M. C. and Yilmaz, Y.: Tethyan evolution of turkey: a plate tectonic approach, *Tectonophysics*, 75, 181–241, 1981.
- 1131 Şengör, A. M. C., Yilmaz, Y., and Sungurlu, O.: Tectonics of the Mediterranean Cimmerides: nature and evolution of the  
 1132 western termination of Palaeo-Tethys, *Geol. Soc. Lond. Spec. Publ.*, 17, 77–112,  
 1133 <https://doi.org/10.1144/GSL.SP.1984.017.01.04>, 1984.
- 1134 Şengün, F., Zack, T., and Dunkl, I.: Provenance of detrital rutiles from the Jurassic sandstones in the Central Sakarya Zone,  
 1135 NW Turkey: U-Pb ages and trace element geochemistry, *Geochemistry*, 80, 125667,  
 1136 <https://doi.org/10.1016/j.chemer.2020.125667>, 2020.
- 1137 Shaanan, U., Avigad, D., Morag, N., Güngör, T., and Gerdas, A.: Drainage response to Arabia–Eurasia collision: Insights from  
 1138 provenance examination of the Cyprian Kythrea flysch (Eastern Mediterranean Basin), *Basin Res.*, n/a,  
 1139 <https://doi.org/10.1111/bre.12452>, 2020.
- 1140 Sharman, G. R., Sharman, J. P., and Sylvester, Z.: detritalPy: A Python-based toolset for visualizing and analysing detrital  
 1141 geo-thermochronologic data, *Depositional Rec.*, 4, 202–215, <https://doi.org/10.1002/dep2.45>, 2018.
- 1142 Sherlock, S., Kelley, S., Inger, S., Harris, N., and Okay, A.: 40Ar-39Ar and Rb-Sr geochronology of high-pressure  
 1143 metamorphism and exhumation history of the Tavsanli Zone, NW Turkey, *Contrib. Mineral. Petrol.*, 137, 46–58,  
 1144 <https://doi.org/10.1007/PL00013777>, 1999.
- 1145 Simonetti, A., Heaman, L. M., Hartlaub, R. P., Creaser, R. A., MacHattie, T. G., and Böhm, C.: U–Pb zircon dating by laser  
 1146 ablation-MC-ICP-MS using a new multiple ion counting Faraday collector array, *J. Anal. At. Spectrom.*, 20, 677–686,  
 1147 <https://doi.org/10.1039/B504465K>, 2005.
- 1148 Smye, A. J. and Stockli, D. F.: Rutile U–Pb age depth profiling: A continuous record of lithospheric thermal evolution, *Earth  
 1149 Planet. Sci. Lett.*, 408, 171–182, <https://doi.org/10.1016/j.epsl.2014.10.013>, 2014.



- 1150 Smye, A. J., Marsh, J. H., Vermeesch, P., Garber, J. M., and Stockli, D. F.: Applications and limitations of U-Pb  
 1151 thermochronology to middle and lower crustal thermal histories, *Chem. Geol.*, 494, 1–18,  
 1152 <https://doi.org/10.1016/j.chemgeo.2018.07.003>, 2018.
- 1153 Spencer, C. J., Kirkland, C. L., and Taylor, R. J. M.: Strategies towards statistically robust interpretations of in situ U–Pb  
 1154 zircon geochronology, *Geosci. Front.*, 7, 581–589, <https://doi.org/10.1016/j.gsf.2015.11.006>, 2016.
- 1155 Stacey, J. S. and Kramers, J. D.: Approximation of terrestrial lead isotope evolution by a two-stage model, *Earth Planet. Sci.*  
 1156 *Lett.*, 26, 207–221, [https://doi.org/10.1016/0012-821X\(75\)90088-6](https://doi.org/10.1016/0012-821X(75)90088-6), 1975.
- 1157 Steiger, R. H. and Jäger, E.: Subcommittee on geochronology: Convention on the use of decay constants in geo- and  
 1158 cosmochronology, *Earth Planet. Sci. Lett.*, 36, 359–362, [https://doi.org/10.1016/0012-821X\(77\)90060-7](https://doi.org/10.1016/0012-821X(77)90060-7), 1977.
- 1159 Storey, C. D., Jeffries, T. E., and Smith, M.: Common lead-corrected laser ablation ICP–MS U–Pb systematics and  
 1160 geochronology of titanite, *Chem. Geol.*, 227, 37–52, <https://doi.org/10.1016/j.chemgeo.2005.09.003>, 2006.
- 1161 Storey, C. D., Smith, M. P., and Jeffries, T. E.: In situ LA-ICP-MS U–Pb dating of metavolcanics of Norrbotten, Sweden:  
 1162 Records of extended geological histories in complex titanite grains, *Chem. Geol.*, 240, 163–181,  
 1163 <https://doi.org/10.1016/j.chemgeo.2007.02.004>, 2007.
- 1164 Sundell, K. E., George, S. W. M., Carrapa, B., Gehrels, G. E., Ducea, M. N., Saylor, J. E., and Pepper, M.: Crustal Thickening  
 1165 of the Northern Central Andean Plateau Inferred From Trace Elements in Zircon, *Geophys. Res. Lett.*, 49, e2021GL096443,  
 1166 <https://doi.org/10.1029/2021GL096443>, 2022.
- 1167 Tang, M., Ji, W.-Q., Chu, X., Wu, A., and Chen, C.: Reconstructing crustal thickness evolution from europium anomalies in  
 1168 detrital zircons, *Geology*, 49, 76–80, <https://doi.org/10.1130/G47745.1>, 2020.
- 1169 Templ, M., Hron, K., and Filzmoser, P.: robCompositions: An R-package for Robust Statistical Analysis of Compositional  
 1170 Data, in: *Compositional Data Analysis*, John Wiley & Sons, Ltd, 341–355, <https://doi.org/10.1002/9781119976462.ch25>,  
 1171 2011.
- 1172 Tera, F. and Wasserburg, G. J.: U-Th-Pb systematics in three Apollo 14 basalts and the problem of initial Pb in lunar rocks,  
 1173 *Earth Planet. Sci. Lett.*, 14, 281–304, [https://doi.org/10.1016/0012-821X\(72\)90128-8](https://doi.org/10.1016/0012-821X(72)90128-8), 1972.
- 1174 Tomkins, H. S., Powell, R., and Ellis, D. J.: The pressure dependence of the zirconium-in-rutile thermometer, *J. Metamorph.*  
 1175 *Geol.*, 25, 703–713, <https://doi.org/10.1111/j.1525-1314.2007.00724.x>, 2007.
- 1176 Topuz, G., Altherr, R., Schwarz, W. H., Dokuz, A., and Meyer, H.-P.: Variscan amphibolite-facies rocks from the Kurtuluş  
 1177 metamorphic complex (Gümüşhane area, Eastern Pontides, Turkey), *Int. J. Earth Sci.*, 96, 861–873,  
 1178 <https://doi.org/10.1007/s00531-006-0138-y>, 2007.
- 1179 Topuz, G., Candan, O., Okay, A. I., von Quadt, A., Othman, M., Zack, T., and Wang, J.: Silurian anorogenic basic and acidic  
 1180 magmatism in Northwest Turkey: Implications for the opening of the Paleo-Tethys, *Lithos*, 356–357, 105302,  
 1181 <https://doi.org/10.1016/j.lithos.2019.105302>, 2020.
- 1182 Triebold, S., von Eynatten, H., Luvizotto, G. L., and Zack, T.: Deducing source rock lithology from detrital rutile geochemistry:  
 1183 An example from the Erzgebirge, Germany, *Chem. Geol.*, 244, 421–436, <https://doi.org/10.1016/j.chemgeo.2007.06.033>,  
 1184 2007.

- 1185 Triebold, S., Luvizotto, G. L., Tolosana-Delgado, R., Zack, T., and von Eynatten, H.: Discrimination of TiO<sub>2</sub> polymorphs in  
 1186 sedimentary and metamorphic rocks, *Contrib. Mineral. Petrol.*, 161, 581–596, <https://doi.org/10.1007/s00410-010-0551-x>,  
 1187 2011.
- 1188 Triebold, S., von Eynatten, H., and Zack, T.: A recipe for the use of rutile in sedimentary provenance analysis, *Sediment  
 1189 Geol.*, 282, 268–275, <https://doi.org/10.1016/j.sedgeo.2012.09.008>, 2012.
- 1190 Ustaömer, P., Ustaömer, T., and Robertson, Alastair. H. F.: Ion Probe U–Pb Dating of the Central Sakarya Basement: A peri-  
 1191 Gondwana Terrane Intruded by Late Lower Carboniferous Subduction/Collision-related Granitic Rocks, *Turk. J. Earth Sci.*,  
 1192 21, 905–932, <https://doi.org/10.3906/yer-1103-1>, 2012.
- 1193 Ustaömer, T., Robertson, A. H. F., Ustaömer, P. A., Gerdes, A., and Peytcheva, I.: Constraints on Variscan and Cimmerian  
 1194 magmatism and metamorphism in the Pontides (Yusufeli–Artvin area), NE Turkey from U–Pb dating and granite  
 1195 geochemistry, *Geol. Soc. Lond. Spec. Publ.*, 372, 49–74, <https://doi.org/10.1144/SP372.13>, 2013.
- 1196 Ustaömer, T., Ustaömer, P., Robertson, A. H. F., and Gerdes, A.: Implications of U–Pb and Lu–Hf isotopic analysis of detrital  
 1197 zircons for the depositional age, provenance and tectonic setting of the Permian–Triassic Palaeotethyan Karakaya Complex,  
 1198 NW Turkey, *Int. J. Earth Sci.*, 105, 7–38, <https://doi.org/10.1007/s00531-015-1225-8>, 2016.
- 1199 Vermeesch, P.: Unifying the U–Pb and Th–Pb methods: joint isochron regression and common Pb correction, *Geochronology*,  
 1200 2, 119–131, <https://doi.org/10.5194/gchron-2-119-2020>, 2020.
- 1201 Vermeesch, P.: On the treatment of discordant detrital zircon U–Pb data, *Geochronology*, 3, 247–257,  
 1202 <https://doi.org/10.5194/gchron-3-247-2021>, 2021.
- 1203 Vry, J. K. and Baker, J. A.: LA-MC-ICPMS Pb–Pb dating of rutile from slowly cooled granulites: Confirmation of the high  
 1204 closure temperature for Pb diffusion in rutile, *Geochim. Cosmochim. Acta*, 70, 1807–1820,  
 1205 <https://doi.org/10.1016/j.gca.2005.12.006>, 2006.
- 1206 Watson, E. B., Wark, D. A., and Thomas, J. B.: Crystallization thermometers for zircon and rutile, *Contrib. Mineral. Petrol.*,  
 1207 151, 413, <https://doi.org/10.1007/s00410-006-0068-5>, 2006.
- 1208 Williams, I. S.: U–Th–Pb Geochronology by Ion Microprobe, in: *Applications of Microanalytical Techniques to Understanding  
 1209 Mineralizing Processes*, Society of Economic Geologists, 1–35, <https://doi.org/10.5382/Rev.07.01>, 1997.
- 1210 Xiong, X. L., Adam, J., and Green, T. H.: Rutile stability and rutile/melt HFSE partitioning during partial melting of hydrous  
 1211 basalt: Implications for TTG genesis, *Chem. Geol.*, 218, 339–359, <https://doi.org/10.1016/j.chemgeo.2005.01.014>, 2005.
- 1212 Yıldız, A., Kibici, Y., Bağcı, M., Dumlupınar, İ., Kocabaş, C., and Aritan, A. E.: Petrogenesis of the post-collisional Eocene  
 1213 volcanic rocks from the Central Sakarya Zone (Northwestern Anatolia, Turkey): Implications for source characteristics,  
 1214 magma evolution, and tectonic setting, *Arab. J. Geosci.*, 8, 11239–11260, <https://doi.org/10.1007/s12517-015-1991-4>, 2015.
- 1215 Zack, T. and Kooijman, E.: Petrochronology and Geochronology of Rutile, *Rev. Mineral. Geochem.*, 83, 443–467, 2017.
- 1216 Zack, T., von Eynatten, H., and Kronz, A.: Rutile geochemistry and its potential use in quantitative provenance studies,  
 1217 *Sediment. Geol.*, 171, 37–58, <https://doi.org/10.1016/j.sedgeo.2004.05.009>, 2004a.
- 1218 Zack, T., Moraes, R., and Kronz, A.: Temperature dependence of Zr in rutile: empirical calibration of a rutile thermometer,  
 1219 *Contrib. Mineral. Petrol.*, 148, 471–488, <https://doi.org/10.1007/s00410-004-0617-8>, 2004b.

1220 Zack, T., Stockli, D. F., Luvizotto, G. L., Barth, M. G., Belousova, E., Wolfe, M. R., and Hinton, R. W.: In situ U–Pb rutile  
1221 dating by LA-ICP-MS: 208Pb correction and prospects for geological applications, *Contrib. Mineral. Petrol.*, 162, 515–530,  
1222 <https://doi.org/10.1007/s00410-011-0609-4>, 2011.

1223 Zoleikhaei, Y., Mulder, J. A., and Cawood, P. A.: Integrated detrital rutile and zircon provenance reveals multiple sources for  
1224 Cambrian sandstones in North Gondwana, *Earth-Sci. Rev.*, 213, 103462, <https://doi.org/10.1016/j.earscirev.2020.103462>,  
1225 2021.

1226